The optimization and analytical characterization of super cavity mirrors for use in the single atom laser experiment

by

Bryndol Avery Sones

B.S., Engineering Physics (1987)
United States Military Academy

Submitted to the Department of Physics
in partial fulfillment of the requirements for the degree of

Master of Science in Physics

at the

MASSACHUSETTS INSTITUTE OF TECHNOLOGY

June 1997

Author .....
Department of Physics
May 30, 1997

Certified by .....
Michael S. Feld
Professor of Physics
Thesis Supervisor

Certified by .....
Kyungwon An
Research Scientist
Thesis Supervisor

Accepted by .....
George F. Koster
Chairman, Departmental Committee on Graduate Students

The optimization and analytical characterization of super cavity mirrors for use in the single atom laser experiment

by

Bryndol Avery Sones

Submitted to the Department of Physics
on May 30, 1997, in partial fulfillment of the
requirements for the degree of
Master of Science in Physics

Abstract

The objective of this thesis is to minimize mirror loss with the goal of constructing a higher finesse resonator for use in future single atom laser experiments. In this thesis, I fully characterize low loss super cavity mirrors in terms of their coefficients of reflection (R), transmission (T), absorption (A), and scattering (S). New techniques for measuring transmission and absorption are introduced leading to the first partitioning of absorption and scattering losses in super cavity mirrors and the first observation of optical bistability induced from absorption in mirror thin-film coatings. Measurements of R and T are done simultaneously with an examination of the cavity ringdown decay while absorption is subsequently measured using the very same experimental configuration. These three measurements then determine S which is identified as the dominant loss mechanism. Finally, with attention focused on scattering, investigations are done to minimize this loss.

Thesis Supervisor: Michael S. Feld
Title: Professor of Physics

Thesis Supervisor: Kyungwon An
Title: Research Scientist

Acknowledgments

My completion of this work at MIT was made possible from the efforts and support of many other people. The first is my wife, Jeannine, who has unconditionally supported me in all aspects of my life and in these two years has shouldered the burden of much of my academic frustrations. My gratitude is given to the US Army and the Department of Physics at West Point whose equal and uniform treatment of its personnel has afforded me numerous career opportunities and the financial support for participation in a graduate physics program. Next, I wish to acknowledge my deepest admiration and appreciation for the four men who most shaped and guided my path through MIT with their academic example, direction, and support. They are Dr. Ramachandra Dasari and Professors Michael Feld, Dan Kleppner, and George Koster. I would also like to thank my colleagues in the Spectroscopy Laboratory; this is truly an extraordinary collection of brilliant people who always made time for my questions about physics and lab equipment. In particular, I am indebted to the camaraderie, collaborations, and intellectual challenges of my friends in the single atom laser group; they include Abdul Aziz Aljalal, Chris Fang-yen, Dr. Bill Quivers, and Changhuei Yang. Finally and most importantly, I must credit my development and progress to Dr. Kyungwon An. As my research supervisor, he patiently endured my slow progress and frequent mistakes. Working endlessly to establish conditions for my success, he was an instrumental figure in the advancement of my knowledge of experimental physics. I am forever grateful for the opportunity to have worked with him.

Contents

List of Figures

List of Tables

Chapter 1

Introduction

The single atom laser was first realized in 1994 at MIT [1]. Perhaps the two most essential elements of this achievement were the demands for strong atom-cavity coupling and a prolonged cavity decay time. Super cavity mirrors were the critical vehicle in reaching these demands. The mirrors' physical structure and cavity length contribute directly to maximizing atom-cavity coupling while their reflectivity contributes to maximizing the cavity decay time.

Since the early 1990's, technological advances in the manufacturing of highly reflective, low loss mirrors have created new opportunities in an unexplored resonator regime. Conventional laser mirrors have typical reflection coefficients of 99% which corresponds to a cavity finesse of a few hundred. In contrast, new super cavity mirrors can now be assembled into a Fabry-Perot optical resonator with a finesse of approximately 1 million. This first generation of super cavity mirrors was necessary to create the single atom laser because of the need for protracted cavity decay time, which means higher finesse.

In general, the single atom laser and its use in future studies in quantum optics and cavity quantum electrodynamics (QED) [2] rest in maximizing the mirror reflection coefficient and hence the cavity finesse. Consequently, mirrors with reflection coefficients approaching 100% are needed. Mirrors can be completely characterized in terms of their reflection (R), transmission (T), absorption (A), and scattering (S) coefficients. By conservation of energy, these four quantities sum to one ($R+T+A+S=1$),

which leads to small values for T, A, S on the order of parts per million (ppm).

Unfortunately, the most treasured reward for the single atom laser is still beyond our grasp. This is the study of the quantum mechanical features of the single atom laser. As discussed in Chapter 2, to push the envelop further, a new generation of mirrors with finesse greater than 3 million is needed. This is increasingly more difficult to achieve because it requires that $T + A + S \leq 1$ ppm.

Furthermore, transmission cannot be too small in order to get a reasonable signal-to-noise ratio in the single atom laser output. The SAL output is proportional to the ratio of T and $(1 - R)$ and, depending on this optimization, A and S must be increasingly smaller. Consequently, absorption and scattering must be well below 1 ppm.

1.1 Overview

The objective of this thesis is to study the absorption and scattering loss mechanisms in super cavity mirrors and to develop strategies to minimize this loss. The motivation of this work is to construct a new improved high-finesse optical resonator for the next series of SAL experiments.

This thesis will devise experimental techniques for completely characterizing super cavity mirrors in terms ofR, T, A, S and develop means for minimizing A and S. By their minimization, the mirror reflectivity as well as the cavity finesse can be maximized.

This work will first discuss the single atom laser and optical resonator in order to establish the motivation for higher cavity finesse and to understand the functional relationship of such cavity parameters as length and mirror radius of curvature. Next, a variety of established techniques for measuring the reflection and transmission coefficients is discussed, leading to R experimentally measured using a cavity ringdown technique [3] and T measured by a ringdown-modified cavity throughput technique.

Absorption and scattering are well known contributors to mirror loss; however, these two factors have never been uniquely partitioned in the description of low loss

mirrors. Typically, absorption and scattering are measured together as loss ($L' = A + S$) [4]. To this point, only photo-thermal spectroscopy techniques have shown promise in measuring relative absorptive losses in low loss mirrors, but these techniques fail in measuring absolute absorption losses because of calibration difficulty [5].

The work of this thesis introduces a simple, nondestructive technique for measuring purely absorptive losses by examining the optical bistability observed in the cavity lineshape of a slowly-scanned, high-finesse cavity [6]. There exists hysteresis in the cavity lineshape depending on whether the scanned cavity crosses resonance while it is expanding or while it is contracting. At resonance, the intra-cavity intensity grows to about a million times the incident intensity, and even small absorption can result in appreciable heating of the mirror. This heating results in thermal expansion of both the mirror thin film and the mirror substrate. While the expansion of the thin film is negligibly small, expansion of the substrate is detectable. Theory applying a tilted Lorentzian lineshape and three dimensional cylindrical thermal diffusion in the substrate results in fitted data used to infer the absorption coefficient.

Scattering is the last mirror characteristic to quantify. Estimates for scattering can be made from the rms surface roughness measurements made with a Mireau Interferometer. While this is often accepted as a reasonable approximation for a scattering measurement, total integrated scattering (TIS) is a direct measurement of scattered light. Here this work employs a modified integrating sphere to make scattering measurements of individual super cavity mirrors.

Finally, once the mirrors are completely characterized, we can identify which loss mechanism contributes most to the total loss. Our attention can then be focused on minimizing the dominant loss using existing mirror processing technology. Optimization can be done by mirror cleaning and mirror redesign. In this work, a centrifuge mirror cleaning apparatus was created which allowed mirrors to be cleaned while mounted on a spinning shaft. A variety of procedures were conducted and evaluated.

A more costly but potentially more fruitful step is to redesign the mirrors themselves by changing the substrate, the radius of curvature, or the composition and/or number of layers in the reflective dielectric thin film stack. This thesis summarizes re-

cent literature, proposes redesign parameters, then experimentally compares original and redesigned mirrors.

The culmination of this work is to synthesize the acquired knowledge of super cavity mirrors in order to construct and test a new super cavity optical resonator with a target finesse of 3 million to be used in the next series of the SAL experiments.

1.2 Organization of Thesis

Chapter 2 is devoted to a discussion of the Single Atom Laser experiment. There I will provide an overview of the single atom laser and a more detailed discussion of the obstacles the project currently faces. This will provide compelling motivation for a higher finesse optical resonator.

In Chapter 3, I present some basic information about resonators and thin films designed for highly reflective mirrors manufacturing.

Chapters 4-7 each discuss the theory and measurement of one of the mirror characteristics: R, T, A, then S. Since R+T+A+S=1, the measurement of three quantities determines all four. This thesis sets out to measure R, T, and A, determine S, then verify S with a subsequent measurement. These four chapters culminate in the super cavity mirrors fully characterized.

In Chapter 8, the results are analyzed and some steps are taken to minimize mirror loss. Included in this chapter is a description of the centrifuge mirror cleaning apparatus and a summary of its advantages and disadvantages. Additionally, some hypotheses about mirror surface roughness and scattering are experimentally tested.

Finally, in Chapter 9, this thesis concludes with a summary of results and a short discussion of future studies.

Chapter 2

Single Atom Laser

The single atom laser (SAL) is termed for the laser oscillation with one atom in a high Q optical resonator. The first, and to this point only, realization of such a device took place in 1994 as the Ph.D. research project of Dr. Kyungwon An. His laser device employs ^{138}Ba atoms excited from the $^1S_0$ ground state to the $^3P_1$ (m=0) excited state by a π-pulse field before entering the cavity. The resulting laser oscillation observed is at 791 nm ($^3P_1 \rightarrow {}^1S_0$) while the mean number of atoms in the cavity varies from 0.1 to 1.0. This results in a mean number of photons inside the cavity changing from 0.14 to 11 [1].

2.1 Photon Generation in SAL

Detailed discussions of the single atom laser are found elsewhere [1][7]. However, any discussion of the single atom laser must include the coherent atom-cavity Rabi interaction, which gives rise to photon generation. Consider a single mode cavity that is injected with a steady flow of barium atoms. Now excite the barium atoms with a pump laser field before they enter the cavity. If the pump laser is tuned to the atom transition to the $^3P_1$ excited state, then the π-pulse excitation can be achieved by adjusting the intensity and mode waist, ω_t of the pump in such a way that the

following condition is satisfied [1]

$$\frac{\Omega_R \omega_p}{v}\sqrt{\pi} = \pi \ , \tag{2.1}$$

where v is the atom velocity, Ω_R is the Rabi frequency of the pump field, and ω_p is the pump beam waist.

For simplicity of discussion, consider perfect π-pulse excitation of the ^{138}Ba atoms so they are completely inverted as they depart the pump field. As the excited atom interacts with the cavity, there is an energy exchange at a Rabi frequency of $2\sqrt{n+1}g$ where n is the number of photons in the cavity, and g is the coupling constant [7]. As the intra-cavity photon number increases, so does the energy exchange rate. Now if the cavity is empty when the excited atom enters, this exchange rate depends solely on the product of the coupling constant and the atom-cavity interaction time, t_{int}. The interaction time is determined by $t_{int} = \sqrt{\pi}\omega_0/v$ where ω_0 is the cavity mode waist. In the current SAL setup, the product gt_{int} is 0.5 radians [8]. These conditions do not satisfy a complete Rabi oscillation of the excited atom. Thereby, the atom is not guaranteed to have exchanged its excitation energy with the cavity, and thus the atom has only a small probability of exiting the cavity in the ground state. See Figure 2-1 for the schematic analogy of the Rabi frequency to the physical pendulum [1].

The exchange of this excitation energy results in a photon left in the cavity. The atom's emission probability, A_{em}, then approaches unity when the Rabi oscillation approaches a half cycle. A_{em} is the same as the probability of finding the atom in the ground state as it leaves the cavity. For exactly n photons in the cavity, this probability is $\sin^2(\sqrt{n+1}gt_{int})$. In general, the steady state photon number in the cavity is described by the photon number distribution function, P_n. We can then write A_{em} as [7]

$$A_{em} = \sum_{n=0}^{\infty} P_n \sin^2(\sqrt{n+1}gt_{int}) \ . \tag{2.2}$$

We can interpret the atom's emission probability, A_{em}, as the efficiency of the system in generating photons. As A_{em} goes to unity, so does the probability that the

Rabi Oscillation

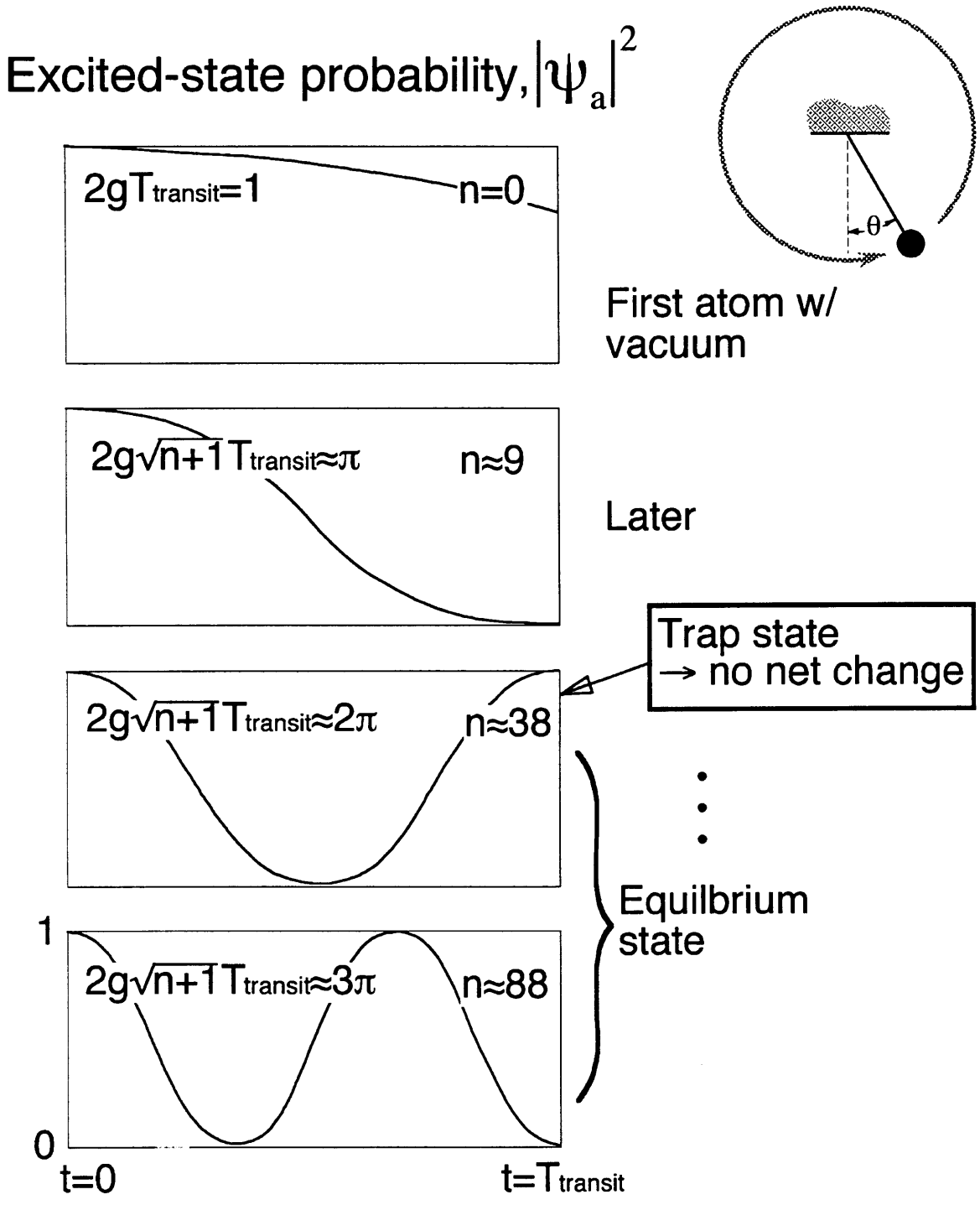

Figure 2-1: Rabi frequency as an analogy to a rotating pendulum.

excited atoms will exit the cavity in the ground state. Our attention is now turned to gt_{int}.

2.2 Maximizing gt

The major obstacles that face the single atom laser's future developments are discussed here. These future developments are in photon/atom statistics and linewidth measurement. Why are these two subjects of interest? Many micromaser theories predict nonclassical photon and atom statistics which often exhibit sub- or super-Poissonian number distributions. While the SAL is a microlaser, these micromaser theories are still applicable to our case. With respects to linewidth, we expect deviation from the Schawlow-Townes limited linewidth under the condition $gt_{int} \gg \pi$. Correlating both the photon statistics and linewidth offers further insight in these truly quantum mechanical features of the single atom laser. Consequently, the reduction of the obstacles rests in meeting this necessary condition to exhibit quantum mechanical features.

The steps to meeting the above condition is to increase g and t_{int}. The atom-cavity interaction time, t_{int}, has dependence on the cavity mode waist and the velocity at which the atom traverses the mode waist. Intuitively, we solve the problem by reducing the velocity and by increasing the mode waist.

The velocity reduction poses a problem because the atom source is a thermal atomic beam which has a Maxwell-Boltzman velocity distribution around a mean of 340 m/s. As a result, there is statistical uncertainty in the velocity of a given atom. Additionally, since the atomic beam is slightly diverging when it reaches the cavity, the atom can have both a longitudinal velocity as well as a transverse velocity in the direction of the the cavity axis. Consequently, the problem is two fold. The atoms must be slowed to a uniform velocity and simultaneously compressed or collimated to eliminate the effect of the transverse velocity component. These two issues are currently being addressed in our laboratory by another researcher employing a velocity selection scheme through optical pumping and collimation with multiple laser beam

compression.

Let's turn now to expanding the mode waist. The mode waist, ω_0, depends on the geometry of the cavity such that

$$\omega_0 = \left(\frac{r_0 L\lambda^2}{2\pi^2}\right)^{1/4}, \tag{2.3}$$

where r_0, L, and λ are the mirror radius of curvature, cavity length, and the probe wavelength, respectively. Then by inspection the mode waist will increase by increasing, L_0, or by choosing more planar mirrors with increased r_0. The unfortunate consequence of these changes in cavity geometry is the reduction of the coupling constant. So we focus our attention to increasing the cavity coupling constant g.

2.3 Demand for Higher Finesse

The increase of g is the motivation of this work. While prolonging t_{int} is not studied in this work, we will see that g and t_{int} are inversely related by the cavity mode waist. In other words, to increase t_{int} with an increase in the mode waist would decrease the optimal coupling constant, g_0, which is defined below

$$g_0 = \frac{\mu}{\hbar}\sqrt{\frac{2\pi\hbar\omega}{V}}, \tag{2.4}$$

where μ is the dipole moment, $\omega = 2\pi c/\lambda$, and V is the mode volume expressed below for the SAL resonator

$$V = \frac{\pi}{4}\omega_0^2 L.$$

And hence, we can write the coupling constant in units of Hz

$$\frac{g_0}{2\pi} = \left(\frac{3}{2\sqrt{2}\pi^2}\right)^{1/2}\sqrt{\frac{c\lambda}{\sqrt{r_0 L^3}}\left(\frac{\Gamma_a}{2\pi}\right)} \tag{2.5}$$

where Γ_a is the atomic free-space spontaneous emission rate. For this particular atomic transition, $\frac{\Gamma_a}{2\pi} = 50$ kHz.

One may wonder why there is a need for higher F when finesse does not appear overtly in the equation for the coupling constant. It can be shown that gt_{int} is independent of r_0 and that for a given F and r_0, there is an optimum cavity length. The optimization of the coupling constant compared to both the atomic emission rate and the cavity linewidth results in $gt_{int} \propto \sqrt{F}$.

First, recall that $t_{int} = \sqrt{\pi}\omega_0/v$. From Equation 2.3, the following relationships can be made

$$t_{int} \propto \frac{(r_0 L)^{1/4}}{v}$$

so that

$$gt_{int} \propto \frac{1}{v\sqrt{L}} . \tag{2.6}$$

Second, the condition for strong atom-cavity coupling requires that

$$2g_0 \gg \Gamma_c, \Gamma_a , \tag{2.7}$$

where Γ_c is the cavity linewidth (FWHM) expressed below

$$\Gamma_c = \frac{c}{L}(1 - R) . \tag{2.8}$$

The requirement expressed in Equation 2.7 demands a parameter ψ to be

$$\psi = \frac{4g^2}{(\Gamma_c + \Gamma_a)^2} \gg 1 , \tag{2.9}$$

and in looking only at the functional dependence and neglecting the constants, we get

$$\psi \propto \frac{\frac{1}{r_0^{1/4} L^{3/4}}}{(\frac{1}{LF} + \Gamma_a)^2} \propto \frac{\sqrt{\frac{L}{r_0}}}{(L + \frac{1}{\Gamma_a F})^2} . \tag{2.10}$$

Then, for a given r_0 and F, ψ is maximized when the two terms in the denominator are about equal, leading to

$$L_{opt} \propto \frac{1}{F} . \tag{2.11}$$

Substituting this expression into ψ and gt_{int}, we get

$$\psi_{opt} \propto \frac{1}{L_{opt}^{3/2} r_0^{1/2}} \propto \frac{F^{3/2}}{\sqrt{r_0}} \tag{2.12}$$

and

$$gt_{int}|_{opt} = \frac{1}{v\sqrt{L_{opt}}} \propto \frac{\sqrt{F}}{v} . \tag{2.13}$$

This noteworthy functional dependence demonstrates the impact of finesse on gt_{int}.

To summarize the above discussion, the goal is to increase gt_{int}. While there is an effort to make improvements in the atomic beam, my focus here is on the resonator. First, there is a trade off for adjustments in the geometry of the resonator. Connected through the cavity mode waist, the coupling constant and t_{int} are competing terms. Consequently, there is an optimum cavity length for a given mirror with finesse, F, and radius of curvature, r_0. Increases in finesse then result in decreases in the optimum cavity length. And, as is shown above, higher gt_{int} is achieved with higher finesse.

2.4 Current SAL Cavity

The single atom laser cavity has three unique qualities. These are its short cavity length, mechanical stability, and length scanning ability. As discussed, in the previous section, there is an optimum cavity length that maximizes atom-cavity coupling. For a cavity finesse of 1 million, optimum cavity length is just 1mm. This short cavity length results in a broad free spectral range. For example, a 1mm cavity has a 150 GHz free spectral range.

This free spectral range gives extreme sensitivity to mechanical instability. The frequency shift $\delta\nu$ due to a cavity length change δL is determined by [1]

$$\delta\nu = \frac{-c}{2L}\frac{\delta L}{\lambda/2} . \tag{2.14}$$

With a 1mm cavity length, a 38 MHz frequency shift follows a length change of

only 1 Å. After some trial and error, Dr. An improved the mechanical stability by housing the resonator assembly in a brass enclosure with large inertia, emplacing Viton o-rings at contact points, and employing teflon screws and spacers to effectively insulate the resonator assembly from surrounding perturbations. The biggest steps toward improved stability came from the simplicity and rigidity of the resonator. The mirrors are glued directly into stainless steel mirror holders machined with a precision of 0.0005 inches. The resonator assembly is further enclosed in a vacuum chamber of pressure of 10^{-7} Torr. The resulting stability is a cavity frequency excursion of only 50 kHz, which is much smaller than the cavity linewidth of 190 kHz .

The last quality of the SAL cavity is the piezoelectric transducer (PZT) which allows for controlled expansion and contraction of the cavity length. The PZT tube is 3/4 inch long, and a Torr-Seal epoxy was applied to the outer edges of the interior so that only the active glue free interior is allowed to expand or contract. The mirror holders are glued to this outer edge of the interior of the PZT tube, thus allowing for both mirrors to move away or towards each other depending on the polarity of the applied voltage on the PZT. Figure 2-2 for schematic of resonator assembly.

2.5 Current SAL Mirrors

The single atom laser mirrors were manufactured by Research Electro Optic, Inc. (REO) in Boulder, Colorado. The pre-manufacturing performance specification were to maximize reflectance with design for 0.5 ppm transmission at the center wavelength of 791 nm. To achieve this goal, the manufacturer chose tantulum pentoxide (Ta_2O_5) and silicon dioxide (SiO_2) for the dielectric thin films and fused silica for the mirror substrate . The substrates are first super polished, then the manufacturer characterizes the surface roughness using a modified Mireau Interferometer. The rms surface roughness is generally at sub angstrom level. The mirrors are then coated with thin films using an ion-beam sputtering deposition technique. The mirror design is such that the there are 45 layers of quarter-wave optical thickness. This traditional high-reflective mirror design is sequenced with alternating high to low refractive index

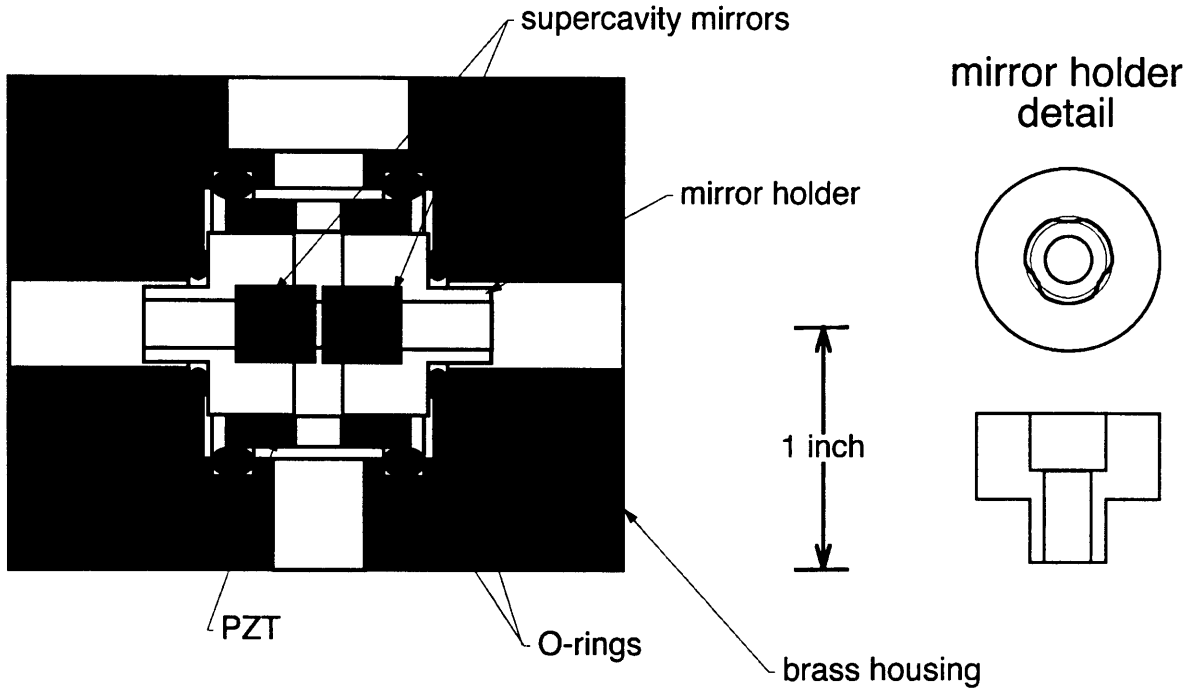

Figure 2-2: The SAL resonator assembly.

material (Ta_2O_5 to SiO_2) ending with a high index. See the figure for optical and thermal properties of the mirror components.

The geometric structure of the mirrors is that the radius of curvature r_0 is 10 cm, the diameter is 4 mm, and the height is 8 mm. The mirror's uncoated end is wedged at a 4 degree angle to the normal in order to distinguish from front and back surfaces during preliminary cavity alignment. Additionally, two variations of mirror surface beveling were done. The manufacturer beveled the mirrors to either 7 degree or 45 degree. This, unfortunately, had to be done after mirror coating and may have some effects on resulting mirror surface roughness.

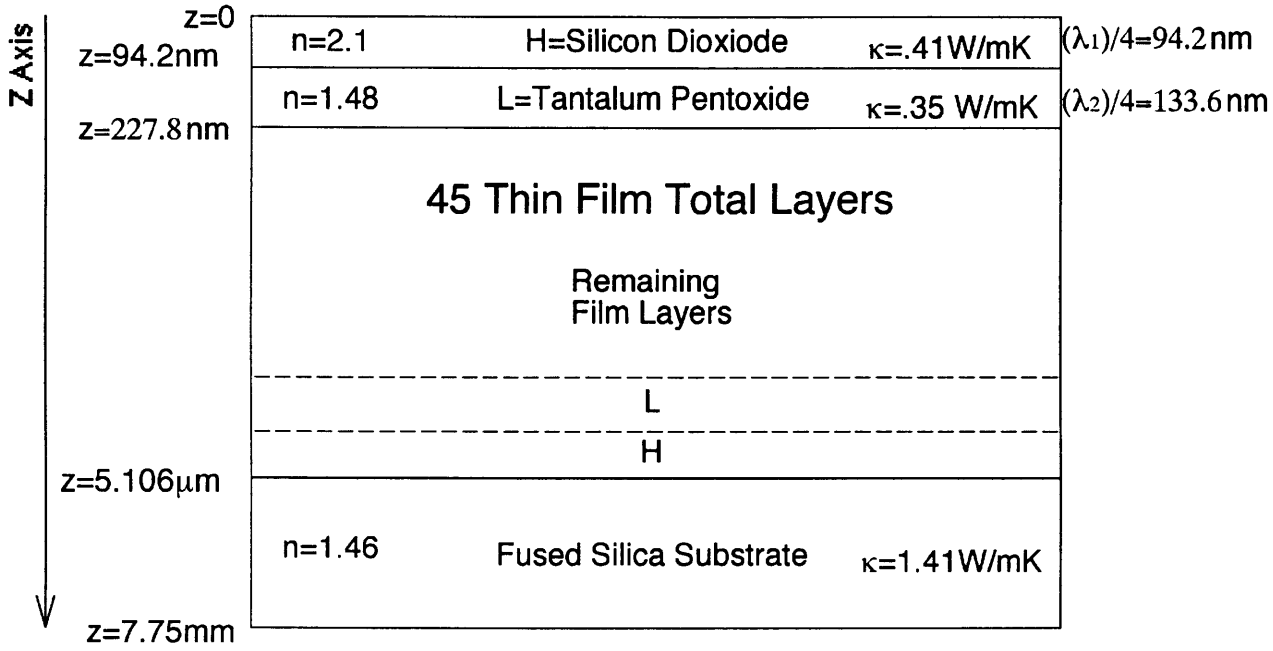

Figure 2-3: Current SAL mirror. κ and n represent the thermal conductivity and index of refraction. Bevel and backside wedge not depicted.

Chapter 3

Thin Film and Resonator Theory

In this chapter, I provide the knowledge needed to understand the design and characteristics of super cavity mirrors and the resonator theory needed to fulfill the resonator-based measurements that allow us to characterize the mirrors. Thin films and their use in manufacturing mirrors is discussed first, followed by the resonator theory.

3.1 Thin Films and Mirrors

With the exception of some polished metals, common laboratory optics such as mirrors, beam splitters, anti-reflective surfaces, and band pass filters are all made with dielectric thin films. Their versatility demonstrates the extremes that can be achieved with appropriate design. For example, two thin film materials can be deposited in such a way to achieve high transmission for a design wavelength in the case of a bandpass filter. Surprisingly, the same two materials can be used for high reflectance resulting in nearly zero transmission. The design differences are in the optical thickness and sequence of the thin films. What follows is a discussion of these two parameters in the design of a highly reflective mirror. Before proceeding, one must understand that the design parameters of thin films emp oy only the opt·· al characteristics of the thin film without regard to scattering due to surface roughness or inter-layer contaminants. This means that loss is only in terms of absorption and that precision in

Index of Refraction	n
Extinction Coefficient	n'
Complex Index of Refraction	N=n-in'
Absorption	$\alpha = \frac{4\pi n'}{\lambda}$
Film Thickness	d
Optical Thickness	$\delta = 2\pi Nd/\lambda$

Table 3.1: Thin film optical parameters.

meeting design parameters depends on the relative magnitude of scattering loss.

3.1.1 Thin Film Properties

Detailed discussion of thin films can be lengthy. While only minimal theory is presented here, readers are referred to H.A. Macleod's "Thin-film optical filters" [9] for additional information. The operations of thin films can be discussed in terms of just a few variables if we limit the discussion to normal incidence. These are listed and defined in Table 3.1.

The essential design parameter for use of thin film is the optical thickness δ of each thin film. The characteristic matrix for a given thin film is

$$[M] = \begin{bmatrix} \cos\delta & (i\sin\delta)/n \\ in\sin\delta & \cos\delta \end{bmatrix} . \tag{3.1}$$

The optical thickness determines the film's effects on propagating light. If the thickness is half-wave ($\delta = \pi$), then the film is tranmissive. In a film of quarter-wave thickness ($\delta = \pi/2$), the film's characteristic matrix is no longer unity.

$$[M]_{1/4} = \begin{bmatrix} 0 & (i/n) \\ (in) & 0 \end{bmatrix} . \tag{3.2}$$

3.1.2 High Reflectance Mirrors

High reflectance can be achieved from an odd number of quarter-wave dielectric thin films with alternating high-low index pairs with a high index film on the outer most sides. Under these circumstances, there is destructive interference at the mirror sur-

face and at each subsequent low to high index interface in the dielectric stack. Conversely, at the high to low index interfaces, there is constructive interference, the magnitude of which decays exponentials through successive layers [10].

The reflectance for a such a mirror with $(2p+1)$ thin film layers is given by [9]

$$R = \left(\frac{1 - \left(\frac{n_H^2}{n_L^2}\right)^{2p} \left(\frac{n_H^2}{n_s}\right)}{1 + \left(\frac{n_H^2}{n_L^2}\right)^{2p} \left(\frac{n_H^2}{n_s}\right)} \right)^2, \tag{3.3}$$

where n_H, n_L, and n_s, respectively represent the high film, low film, and substrate indexes of refraction. Then we see that with more layers, there is higher reflectance. Additionally, as with the case of the SAL cavity mirrors

since

$$\left(\frac{n_H^2}{n_L^2}\right)^{2p} \frac{(n_H^2)}{(n_s)} \gg 1 \tag{3.4}$$

then

$$R \approx 1 - 4\left(\frac{n_L^2}{n_H^2}\right)^{2p} \frac{n_s}{n_H^2} \tag{3.5}$$

and for a lossless mirror

$$T = 1 - R \approx 4\left(\frac{n_L^2}{n_H^2}\right)^{2p} \frac{n_s}{n_H^2} \tag{3.6}$$

As seen from the above equation, the addition of one more L-H index pairs increases the reflectance and in doing so, reduces the transmittance by a factor of $(n_L/n_H)^2$. This equates to a reduction of 50% in T for each additional thin film pair added to the SAL mirrors.

3.1.3 Quarterwave Optimization and High Reflectance Zones

Thin film dielectric films have two inherent defects. Both arise from operations at wavelengths other than the design wavelength, λ_0. The first is that the optical path length can be complicated by phase changes at either end of a particular film. The

second is that their high reflectance is for a limited band of wavelengths around the design wavelength.

Using the Fabry-Perot model for thin films, let ϕ_a and ϕ_b be the phase change at either boundary of the thin film. Then peak transmissions occur under the following conditions

$$\frac{\phi_a + \phi_b - 2\delta}{2} = q\pi \qquad \text{where} \qquad q = 0, \pm 1, \pm 2 \ldots \tag{3.7}$$

The effects of this problem is to shift the transmission peak wavelength slightly. As introduced in 1964, this problem can be easily overcome with the use of two different film thicknesses [11]. More recent analysis also discusses the need for some layers that are slightly different than quarter-wave thick. C.K. Carniglia *et al.* report the need to modified thin film optical thickness relative to the reflectance of the preceeding film pair. Designing for maximum reflectance given slight absorption, they found that it was necesary to increase the low index (n=1.47) films to 1.4 quarter-wave thickness, while the high index (2.35) films were reduced to 0.7 quarter-wave; half-wave thichness for the low-high pair was still necessary [12].

The second inherent defect is the wavelength range for high reflectance. While highly reflective within this range, the mirror can become nearly transparent for wavelengths outside of the range. The full width of the zone $2\frac{\Delta\lambda}{\lambda_0}$ is expressed below [9]

$$\frac{\Delta\lambda}{\lambda_0} = \frac{2}{\pi}\sin^{-1}\left(\frac{n_H - n_L}{n_H + n_L}\right). \tag{3.8}$$

Then for the SAL mirrors the high reflectance zone would be 791 nm $\pm$ 88 nm. This determines the zone for λ_0. However, the criteria for high reflection is odd number of layers of quarter wave thickness. This allows for high reflection at λ_0, $\lambda_0/3$, $\lambda_0/5$, and so on.

3.1.4 Absorption Losses in Thin Films

Thin film optical absorption is estimated at the microscopic level by summing the absorption in each individual thin films to determine the absorption losses for the entire assembly. Analysis is done with the potential transmittance of each film. Unlike

Reflection Coefficient	.9999997
Finesse	11 Million
Transmission	0.3 ppm
Absorption	*0.28 ppm*(see note below)
High Reflectance Zone	791 nm $\pm 100nm$

Table 3.2: Thin film theory predictions for SAL mirrors.

throughput, this quantity is the ratio of transmitted intensity to only the entering intensity of a thin film. The expression for absorption in a quarter-wave stack, with the final layer a high index film, is given by [9]

$$A = \frac{2\pi n_0(n'_H + n'_L)}{(n_H^2 - n_L^2)}, \tag{3.9}$$

where n_0 is the index of the incident material, which is often air, and n'_L and n'_H represent the thin film extinction coefficients.

3.1.5 Theory's Prediction for SAL Mirrors

The application of thin film theory to the current SAL mirrors then predicts the results found in Table 3.2. Again, an important comment about these theoretical predictions is that scattering losses are not incorporated into the thin film mirror design formulae.

Note that the extinction coefficients (Ta_2O_5) and (SiO_2) are not well known. The manufacturer has reported that both extinction coefficients were zero to six significant figures [13]. I assumed values of $n'_L = n'_H = .5 \times 10^6$ for the values in the table.

3.2 Optical Resonators

Our discussion of optical resonators starts at a rudimentary level to lay the foundation for more complicated analysis of the single atom laser resonator. The approach here is to first discuss the propagation of a Gaussian beam in a homogeneous medium and then discuss a lossless Fabry-Perot interferometer. This will lead to definitions of higher order mode structures in a resonator, the resonator stability conditions.

and characteristic qualities for the SAL resonator. A more detailed discussion can be found in A. Yariv's "Quantum Electronics" [14].

3.2.1 Gaussian Beams in Resonators

In this section, we define the Gaussian beam, apply the Gaussian beam formalism to an optical resonator, then discuss the fundamental and higher order modes of the Gaussian beam inside of the resonator.

The Gaussian beam is one in which the intensity distribution at planes normal to the direction of propagation is described by a Gaussian function of the radial coordinate r. This is the most common of laser beams. Let's first define the beam propagation to be in the z-direction and that $r^2 = x^2 + y^2$. Furthermore, let's assume that the electric field varies only in the r and z directions and that there is no azimuthal dependence on the cylindrical coordinate ϕ. Then we can define the the Gaussian beam electric field in terms of three well known Gaussian beam parameters, $\omega(z)$ the beam waist, $R(z)$ the beam radius of curvature, and $\nu(z)$ the beam slope.

$$E(x,y,z) = E_0 \frac{\omega_0}{\omega(z)} exp\left\{-i[kz - \nu(z)] - r^2\left(\frac{1}{\omega^2(z)} + \frac{ik}{2R(z)}\right)\right\} , \qquad (3.10)$$

where $k = 2\pi/\lambda$ with λ the wavelength of the light, and $\omega(z)$ is the distance off the z-axis at which the field amplitude drops to 1/e. These three parameters are defined below with n the index of refraction of the resonator medium:

$$\omega^2(z) = \omega_0^2\left[1 + \left(\frac{\lambda z}{\pi\omega_0^2 n}\right)^2\right] = \omega_0^2\left(1 + \frac{z_0^2}{z^2}\right) ,$$

the radius of curvature $R(z)$

$$R(z) = z\left[1 + \left(\frac{\pi\omega_0^2 n}{\pi z}\right)^2\right] = z\left(1 + \frac{z_0^2}{z^2}\right) ,$$

the slope $\nu(z)$

$$\nu(z) = \tan^{-1}\left(\frac{z}{\pi\omega_0^2 n}\right) = \tan^{-1}(\frac{z}{z_0}) ,$$

and the confocal parameter z_0 given by

$$z_0 = \frac{\pi\omega_0^2 n}{\lambda} .$$

Now consider when there is azimuthal dependence of the electric field. This allows for the higher modes of the Gaussian beam. As a result, the electric field is then described by the following expression

$$\begin{aligned} E_{l,m}(x,y,z) &= E_0 \frac{\omega_0}{\omega(z)} H_l H_m \left(\sqrt{2}\frac{x}{\omega(z)}\right)\left(\sqrt{2}\frac{y}{\omega(z)}\right) \\ &\quad \exp\left[-ik\frac{x^2+y^2}{\omega^2(z)} - \frac{ik(x^2+y^2)}{2R(z)} - ikz + i(l+m+1)\nu\right] \end{aligned} \quad (3.11)$$

where H_l and H_m are the Hermite polynomials of the respective orders, l and m. From this expression, comes the notion of Transverse Electric Magnetic modes, $\mathrm{TEM}_{l,m}$.

The stability condition for the resonator is given by

$$0 \leq (1 - \frac{L}{R_1})(1 - \frac{L}{R_2}) \leq 1 , \quad (3.12)$$

where L is the cavity length and R is the mirror's radius of curvature. The SAL resonator clearly meets this condition ($R_1 = R_2 = r_0$=10 cm, L =1 mm).

3.2.2 Fabry Perot Interferometers

At this point, I wish to derive some resonator characteristics. It is best to elucidate these ideas with the Fabry-Perot interferometer with flat, lossless reflectors. When we speak of lossless resonators, we restrict ourselves to the stable resonator whose internal Gaussian beam is completely confined or coupled to the resonator and to the condition for no loss from absorption and scattering. In this criteria, the lossless resonator obeys the conservation of energy relationship of

$$R + T = 1 .$$

Consider first the simple case of two plane reflectors separated by a distance L. This is a Fabry-Perot etalon or more often called an interferometer for its frequent functional use. Let the plane reflectors be aligned such that the reflected beams retrace over themselve. There are multiple reflected and transmitted beams created from multiple round trips in the internal medium. The phase delay between two round trips is given by

$$\delta = \frac{4\pi n L}{\lambda} \tag{3.13}$$

where n is the index of refraction of the Fabry-Perot medium. Consequently, the reflected beam is the superposition of these multiple reflected beams and likewise the transmitted beam is the superposition of the multiple transmitted beams. Their superposition is governed by this phase delay δ as it determines the interference of these beams. Then we can express the reflectance as ratio of reflected to incident intensity

$$\frac{I_r}{I_i} = \frac{4R\sin^2(\frac{\delta}{2})}{(1-R)^2 + 4R\sin^2(\frac{\delta}{2})}\,, \tag{3.14}$$

and the transmittance, as the ratio of the transmitted to incident light

$$\frac{I_t}{I_i} = \frac{(1-R)^2}{(1-R)^2 + 4R\sin^2(\frac{\delta}{2})}\,. \tag{3.15}$$

Inspection of the sine arguments in the above equations show that reflectance can drop to zero and transmitance can grow to unity depending on δ. The transmission will go to 100% when $\delta = 2m\pi$ for m=any integer. Then in terms of optical frequency, $\nu = \frac{c}{\lambda}$, maximum transmission occurs when

$$\nu_m = m\frac{c}{2nL}\,, \tag{3.16}$$

and hence defining a free spectral range (FSR) as

$$\Delta\nu \equiv \nu_{m+1} - \nu_m = \frac{c}{2nL}\,. \tag{3.17}$$

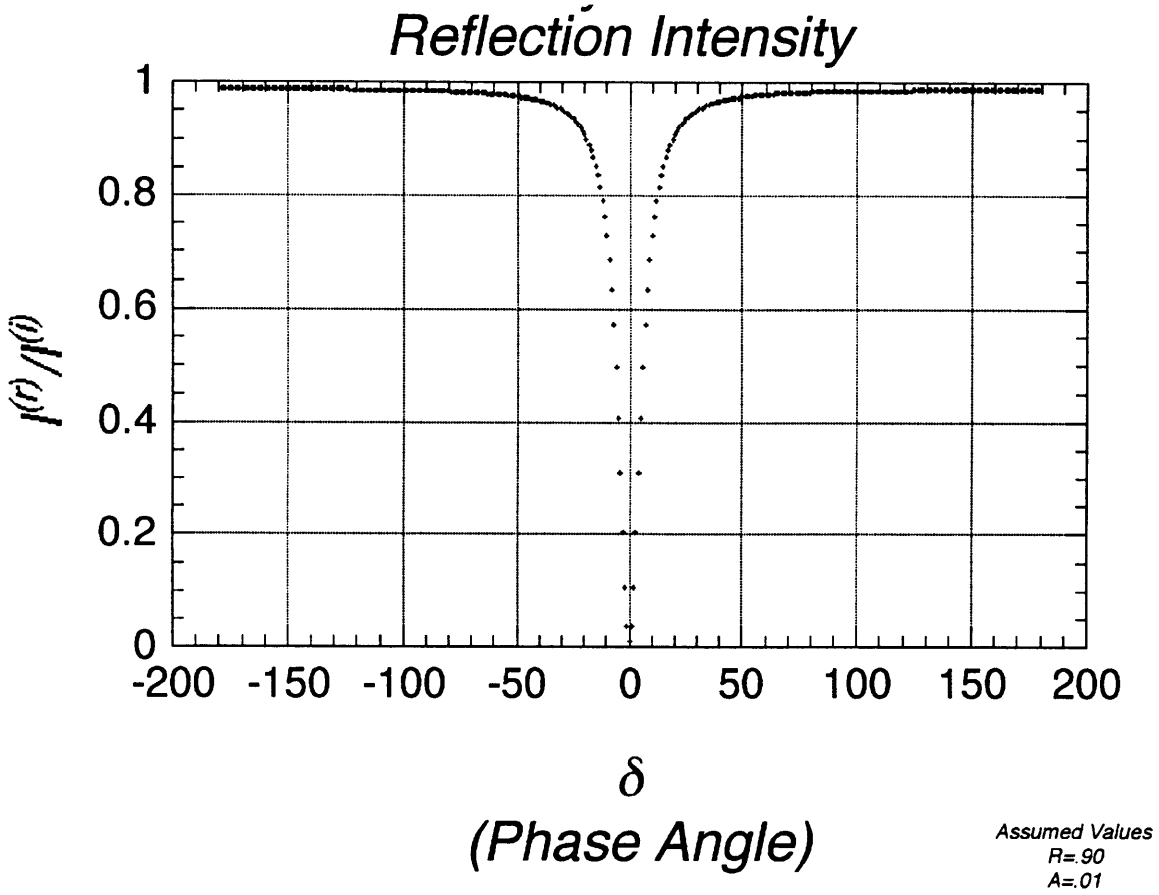

Figure 3-1: Fabry-Perot reflection dependence on phase angle for R=0.90 and A=0.01.

3.2.3 Definition of Finesse

The above expression demonstrates the relationship of the resonance frequency ν with the length L. This relationship offers the value of Fabry-Perot etalons as spectrum analyzers and leads to the definition of the Fabry-Perot characteristic termed "finesse." Differentiating the above equation gives

$$\frac{d\nu}{\Delta\nu} = -\frac{dL}{(\lambda/2n)} \tag{3.18}$$

We see that changes in the separation length by half wavelengths then changes the resonance wavelength by a FSR. However, there are resolution problems if the width of these transmission maximums are comparable to the spacing between adjacent transmission maximums. The term finesse is introduced to quantify the resolving power of the Fabry Perot.

$$F \equiv \frac{\pi\sqrt{R}}{1-R} \approx \frac{\pi}{1-R} \tag{3.19}$$

The above equation demonstrates the direct relationship between reflectivity and resonator finesse. With highly reflective mirrors, common convention is to express the resonator mirrors' reflectivity in terms of finesse since R is so close to unity.

The separation is defined as the frequencies at which the transmission is reduced to half its maximum peak. This occurs when the two terms in the denominator in Equation 3.15 become equal to each other

$$\sin^2\left(2\pi\delta\nu_{1/2}nL/c\right) = \frac{(1-R)^2}{4R}\,.$$

With the assumption of $\delta\nu_{1/2}L/c \ll \pi$, we then have

$$2\delta\nu_{1/2} \approx \frac{c}{2\pi nL}\frac{1-R}{\sqrt{R}}\,. \tag{3.20}$$

The result is a defining equation for finesse as the ratio of the separation between transmission peaks to their width.

$$F = \frac{\Delta\nu}{2\delta\nu_{1/2}} = \frac{\text{FSR}}{\text{FWHM}} \tag{3.21}$$

3.2.4 Single Atom Laser Resonator

The SAL resonator is built such that the cavity length is much shorter than the mirror radius of curvature. In this design, the goal is to achieve laser oscillation at a single frequency. Some key parameters in the single mode resonator are listed below.

$$\text{Confocal Parameter} \qquad z_0 = \sqrt{\frac{r_0 L}{2}} \tag{3.22}$$

$$\text{Transverse Mode Spacing} \qquad \Delta\nu_t = \frac{c}{2\pi z_0} \quad \text{if } r_0 \gg L \tag{3.23}$$

$$\text{Cavity Mode Waist} \qquad \omega_0 = \sqrt{\frac{z_0\lambda}{\pi}} \tag{3.24}$$

$$\text{Coupling Constant} \qquad \frac{g_o}{2\pi} = \left(\frac{2}{2\sqrt{2}\pi^2}\right)^{1/2} \sqrt{\frac{c\lambda}{\sqrt{r_0 L^3}}\left(\frac{\Gamma_a}{2\pi}\right)} \tag{3.26}$$

$$\text{Interaction Time} \qquad t_{int} = \frac{\sqrt{\pi}\omega_0}{v} \,. \tag{3.27}$$

With the mirror and resonator properties discussed, we can employ these principles in the measurement of R, T, A, and S. The next four chapters discuss the particular theory and measurement of these quantities.

Chapter 4

The Reflection Coefficient

This chapter discusses the theory for the three different techniques for measuring the reflection coefficient, then employs the ringdown technique for measuring R.

4.1 Reflection Theory

The measurement of the reflection coefficient most often involves the measurement of cavity finesse because of its direct relationship to R. Three distinct techniques for measuring the cavity finesse are presented here. The first uses the knowledge of the ringdown modulation period and amplitude to develop a linear relationship, from which cavity finesse can be extracted. The other two techniques measure the cavity decay time to determine the cavity finesse. This section discusses the cavity ringdown modulation followed by subsection for each of the three techniques for measuring finesse.

4.1.1 Cavity Ringdown

This theory is primarily taken from Reference [3]. In a scanned Fabry-Perot resonator, there is a time dependent cavity length given by

$$L(t) = L_0 + vt \tag{4.1}$$

where L_0 is the cavity length at $t = 0$ and v is the mirror velocity. If a monochromatic laser beam probes the cavity, the resulting electric field inside the cavity at any given time can be expressed as

$$E_{in}(t) = E_0 e^{i(kz-\omega t)} \sum_{n=0}^{\infty} r^{2n} e^{i2nk[(1-n\frac{v}{c})L_0+vt]} . \tag{4.2}$$

The effect is a doppler shift in the frequency of the propagating field between successive round trips in the cavity. The result is that the internal intensity has a characteristic exponential decay with a superimposed ringdown modulation.
The decay is given by

$$I_{in}(t) \propto e^{-2(1-R)\frac{ct}{2L}} = e^{-\Gamma_c t}. \tag{4.3}$$

The modulation is given by

$$I_{in}(t) \propto R^{2l} \left| \sum_{n''=1}^{l} r^{-2n''} e^{-ikv(\frac{2L_0}{c})n''^2} + \sum_{n'=0}^{\infty} r^{-2n'} e^{-ikv(\frac{2L_0}{c})n'^2} \right|^2 . \tag{4.4}$$

In the above expression, k is the wave number, c is the speed of light, and the index l represents an arbitrary time t given by $t = \frac{2L_0}{v} l$. The second summation represents the initial field, and the the first summation represents the time dependent modulation of this cavity field. The significance of the above relationship is that the phase of the exponential in the first summation characterizes the frequency of the ringdown modulation. The mth "minimum" of this modulation is determined by

$$t_m = \sqrt{m(\frac{2L_0}{c})(\frac{\lambda}{v})} . \tag{4.5}$$

For example, the time between the first and second minima is

$$T_{12} \equiv t_2 - t_1 = (\sqrt{2} - 1)\sqrt{(\frac{2L_0}{c})(\frac{\lambda}{v})} . \tag{4.6}$$

See Figure 4-1 for T_{12}.

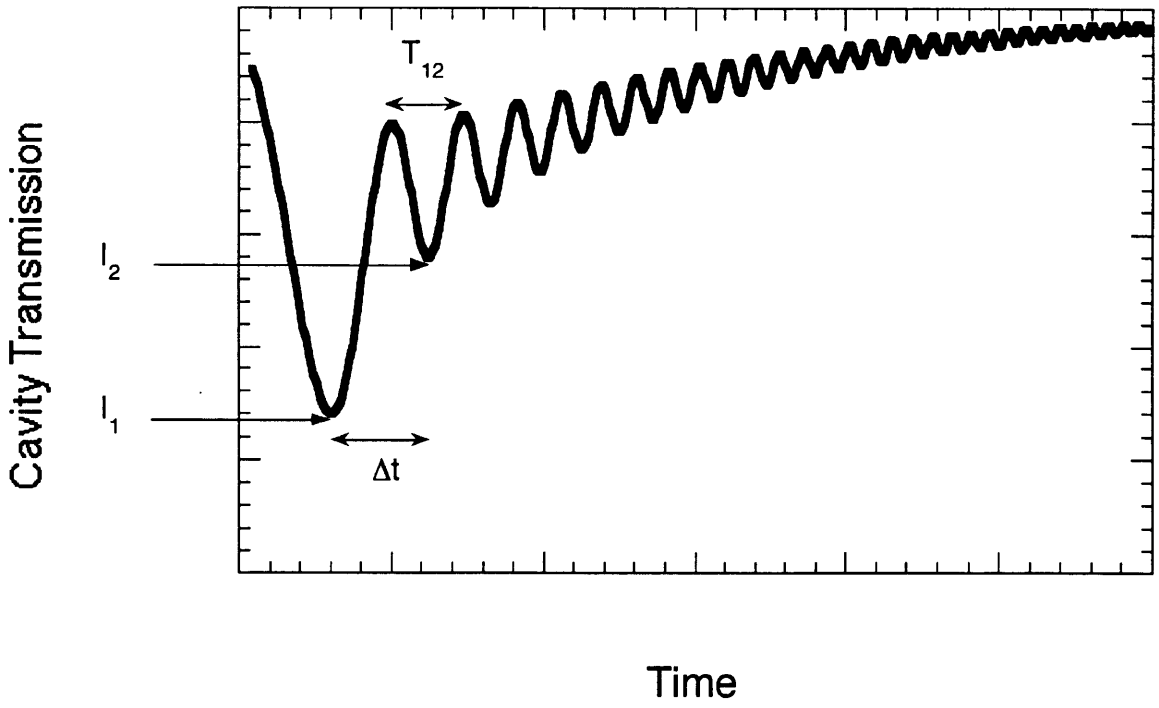

Figure 4-1: Theoretical ringdown modulation defining parameters T_{12}, Δt, I_1, I_2.

4.1.2 Measurement of Finesse from Ringdown Modulation

Similar to the above analysis of the modulation frequency, J. Poirson *et al.* analyzed the ringdown modulation using the error function [15] and then described the time between the first and second amplitude maximum with

$$\Delta t = (\sqrt{5} - 1)\sqrt{\frac{L_0 \lambda}{2vc}} \,. \tag{4.7}$$

The intensity of the first and second maxima, I_1 and I_2 respectively, are related in the following manner

$$\frac{I_1}{I_2} = \exp(\frac{\Delta t}{\tau}) \approx e\frac{\Delta t}{\tau} \tag{4.8}$$

with e the numerical value $e = 2.7$. So that using the definition of cavity decay time, the following can be used to relate Δt, F, and I_1/I_2 in the vicinity of $\Delta t \approx \tau$ [15]

$$\frac{\pi c}{L_0}\Delta t \approx \frac{F}{e}\frac{I_1}{I_2} \,. \tag{4.9}$$

The utility of this relationship is that when $\frac{I_1}{I_2} = e$, then $\frac{\pi c}{L_0}\Delta t = F$. So if data is collected for I_1, I_2, and Δt for a variety of cavity scan speeds, the graphical determination of F can be made from the plot of $\frac{\pi c}{L_0}\Delta t$ versus $\frac{I_1}{I_2}$. The corresponding value at $\frac{I_1}{I_2} = 2.7$, then determines F. These measurements of finesse are reported to be accurate to 1%[15].

The advantages in using this technique are that (1) it demonstrates reasonable predictions of the temporal and amplitude behaviour of the ringdown modulation and (2) it can serve as a validation for an independent finesse measurement. However, the problem in this technique is that it is time consuming to take at least three data points and graphically determine the finesse. A viable option to this problem is to measure the finesse immediately with one measurement of the cavity decay time.

4.1.3 Cavity Decay with a Shuttered Probe

In the previous measurement technique, multiple data points are needed to create the graphical determination of finese. An examination of the cavity decay time is a more direct means of determining finese in one single measurement. Finese is related to the cavity decay time t_c by the following

$$F = \frac{t_c \pi c}{L_0} . \tag{4.10}$$

In a hallmark experiment in 1992, G. Rempe *et al.* devised an experiment for measuring the cavity decay time for a resonator made with low loss mirrors. They report the highest finesse measured to this date, with F=1.9 x 10^6 [4]. This corresponds to a R=0.9999984 and T+A+S=1.6 ppm. While the electronics of this experiment may pose some complication, the concept is simple. An acousto-optic switch (AOS) provides the ability to shutter the probe laser beam as the cavity is slowly scanned with a PZT. The cavity length is changed slowly allowing the probe beam to come into resonance with a cavity TEM_{00} longitudinal mode. The transmission detection scheme is preset to a threshold signal that triggers the AOS to turn off the probe beam in approximately 45 ns. The resulting transmission signal records the decay of

Cavity Length	4 mm
Wavelength	850 nm
Radius of Curvature	17.3 cm
Thin Films	Ta_2O_5 and SiO_2
Film Layers	45
Substrate	FS
Coating Manufacturer	PMS
Substrate Manufacturer	General Optics

Table 4.1: Mirror and experimental parameters resulting in F=1.9 x 10^6.

the cavity field. The decay time is determined by measuring the time it takes the cavity field to decay to 1/e of its maximum value.

Some important parameters of this experiment are shown in Table 4.1. The coating manufacturer PMS is the same company that manufactured the single atom laser mirrors. Their name has changed to Research Electro Optics, Inc. The above experiment was also done with PMS fused silica substrates with radius of curvature of 100 cm. Reference [4] makes no note of the performance of the PMS BK7 substrates, although PMS reports similar performance [13].

4.1.4 Cavity Decay without a Shuttered Probe

Still a simpler approach to measuring the cavity decay time is to scan the cavity at an even faster frequency [1]. This eliminates the need for the optical shutter discussed in the previous section. The effect is a delta function-like injection of the probe laser beam when the cavity length sweeps by the resonant condition of the TEM_{00} longitudinal mode. As discussed above, the measurement of the cavity decay time determines the finesse, which then determines the reflection coefficients of the cavity mirrors. But recall, from Eq. (4.4), that there are two effects of the scanning cavity. In this case, the desirable characteristic is the exponential decay while the superimposed modulation can interfere with the precise measurement of the decay time. The goal is then to minimize the amplitude modulation.

In general, the slower the cavity scan, the larger the amplitude of modulation and the larger the time interval between the first and second minima in the cavity

transmission. It is in this regime that the modulation dominates the exponential decay characteristics. Then it is necessary to scan the cavity at a mirror velocity such that $T_{12} \ll t_c$.

The scan velocity can be chosen by trial and error. However, since we know that the cavity finesse is approximately 1 million, some preliminary predictions of the cavity decay time and a suitable scan speed can be chosen before going to the laboratory. With the single atom laser resonator, we can then predict a cavity decay time using Eq. (4.10) to be about 1μs. Then let $100T_{12} = t_c$; the corresponding mirror velocity is about 10 μ m/s to meet the condition for eliminating the effects of the ringdown modulation.

In order to scan the cavity around this mirror velocity, it is necessary to convert the scan frequency (frequency per time) to velocity. The velocity $\frac{dL}{dt}$ is determined from the cavity scan frequency $\frac{d\nu}{dt}$

$$\frac{dL}{dt} = \frac{-\lambda L_0}{c}\frac{d\nu}{dt} . \tag{4.11}$$

Once an appropriate mirror velocity is set, the precise measurement of the cavity length L_0 can complete the finesse measurement. This can be determined by the transverse mode spacing using Eq. (3.23). With t_c and L_0 measured, F can be determined using Eq. (4.10).

4.2 Measurement of R

The cavity ringdown technique described in Section 3.1.5 is used to measure the finesse which determines R from $R = 1 - \pi/F$. The cavity is scanned by applying a ramp voltage of 135 V to the PZT. Depending on the polarity of the voltage, the effects of this applied voltage serve to either contract or expand the PZT and hence the cavity length. In this case, the ramp voltage was generated from a Textronix analog osciloscope and the polarity of the applied voltage was such that the cavity expands across resonance as the applied voltage climbs the ramp.

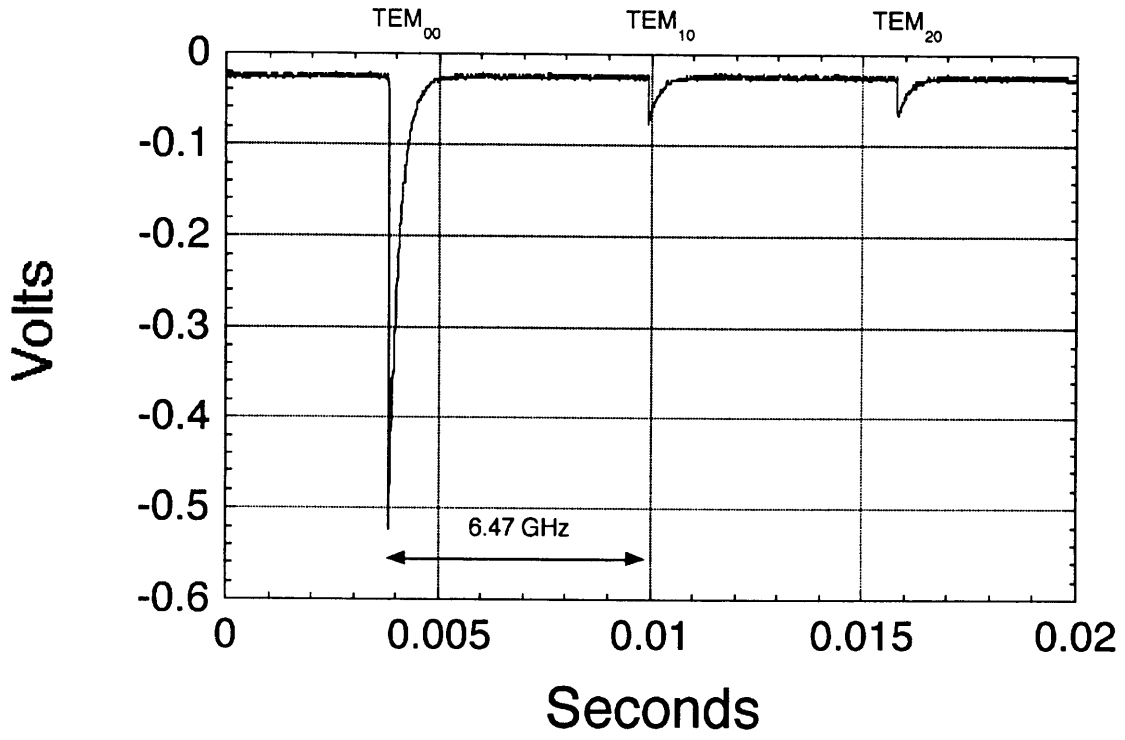

Figure 4-2: Cavity transverse mode spacing=6.47 GHz.

The variable in this measurement is the scan speed. Recall that the amplitude of the cavity transmission and the modulation from the ringdown is a function of the scan speed. As a general rule, the cavity alignment and the coupling of the pump beam to the TEM_{00} mode are done with a slow scan while data is later taken at a faster scan in order to minimize the modulation in the cavity decay signal. For finesse measurements of a 1 mm cavity, the scan speed was typically around 6 GHz/ms which corresponds to a mirror velocity of 16 μm/s.

While the cavity length is designed for 1 mm, exact measurements of the length must be done to accurately determine finesse. This is done by examining the transverse mode spacing. The length can be determined using Eq. (3.23). This leads to the following

$$L_0 = \left(\frac{c}{2\pi\Delta\nu}\right)^2 \frac{2}{r_0}. \tag{4.12}$$

The mode spacing is measured on the analog oscilloscope. This measurement provides the time between modes, and the time can be easily calibrated to frequency by shift-

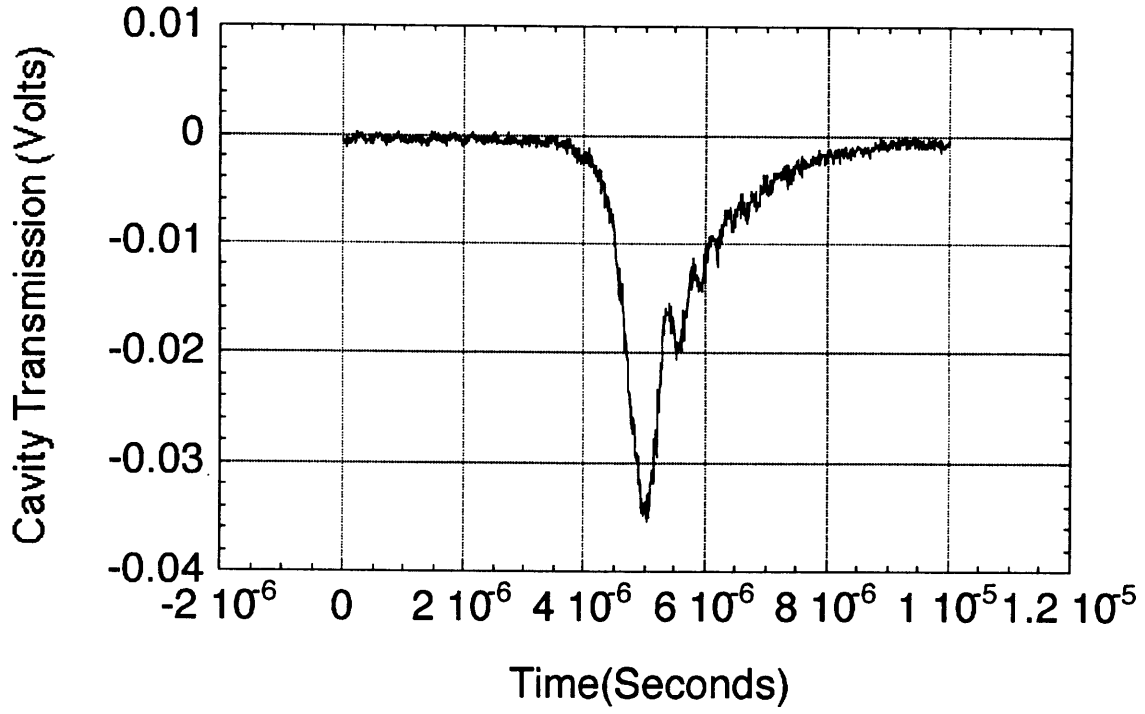

Figure 4-3: SAL cavity transmission. Finesse=9.00 $\times 10^5$.

ing the pump laser by a known offset frequency to determine the time-to-frequency conversion. For example, as seen in Figure 4-2 the spacing is determined to be 6.47 GHz, which results in a cavity length of 1.06 mm.

As a demonstration of the determination of the decay time, I show data for the SAL cavity and another low loss cavity measured in the lab. The SAL finesse is lower due to a typical degradation from deposited barium atoms. Transmission for the two cavities are shown in Figures 4-3 and 4-4. With cavity length determined, the measurement of cavity decay time then leads directly to the finesse measurement by the relationship in Eq. (4.10).

Recall that the decay time is the time in which the cavity intensity decays to $1/e$ of its maximum value at resonance. The amplitude of the cavity transmission is converted to a logarithmic plot to simplify this measurement. In Figures 4-5 and 4-6, I demonstrate the log plots of the SAL and the other cavity transmission. Data is then fit in the linear portion of this curve in order to minimize the effects of the ringdown modulation. This fit line then determines the decay time as the time to decrease by

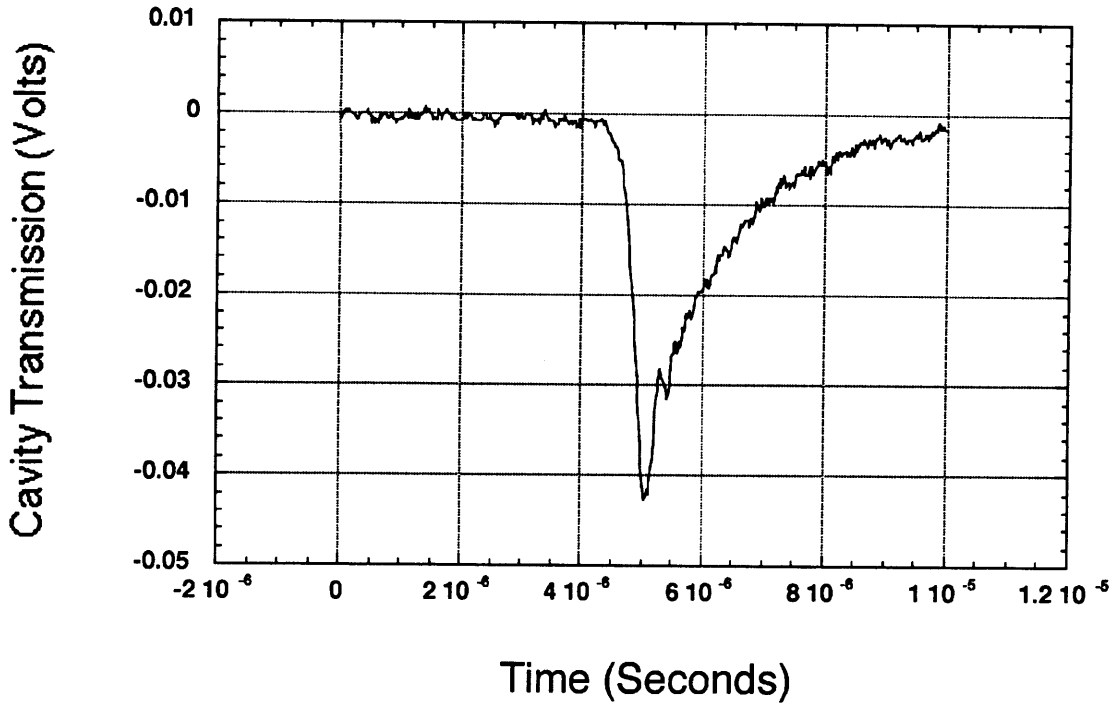

Figure 4-4: Cavity transmission for another mirror pair. Finesse=1.32 $\times 10^6$.

one division $(1/e)$. Repeated finesse measurements result in some statistical variation such that the finesse for the single atom laser resonator is $F = 9.0 \pm 0.1 \times 10^5$.

In an attempt to validate the finesse measurement from the "ringdown modulation" technique, I used the graphical technique to measure the finesse of a separate resonator. Here the finesse was measured to be 910,000 while the current method determined a finesse of 900,000. Figure 4-7 shows the data collected for this measurement. The graph shows six data points for different scan speeds, with slower scan speeds resulting in a higher I_1/I_2 ratio. One valued observation from this data is the fact that it looses its expected linearity at slower scan speeds. This was our first observed indication of thin film heating at slow scans. The technique is an appropriate check of other finesse measurements; however, since at least three data points are needed to create the finesse graph, a single measurement of the decay time is a much more efficient way to determine the finesse.

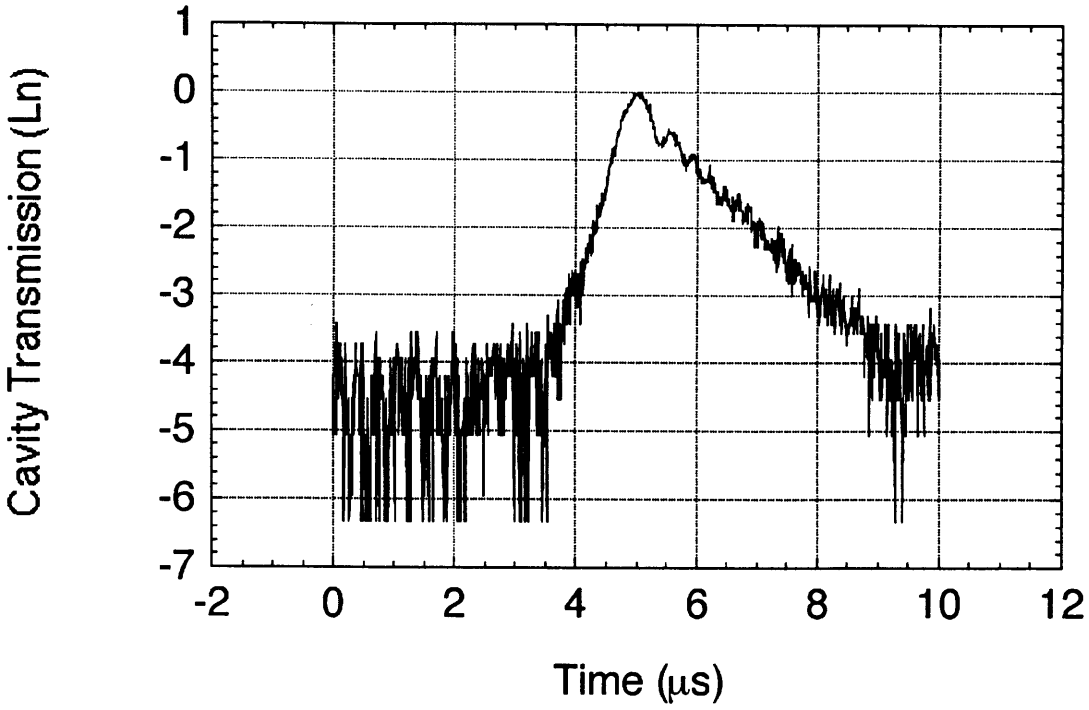

thes/fin1

Figure 4-5: SAL cavity transmission log plot.

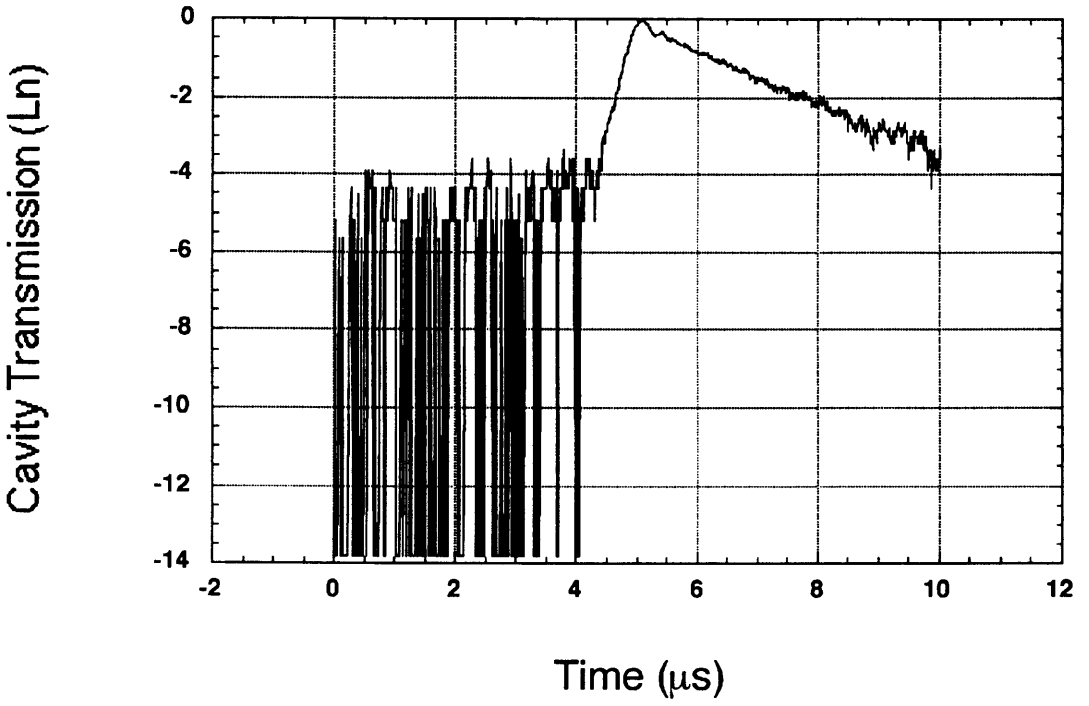

cav14b.log

Figure 4-6: Log plot of cavity transmission for determination of decay time.

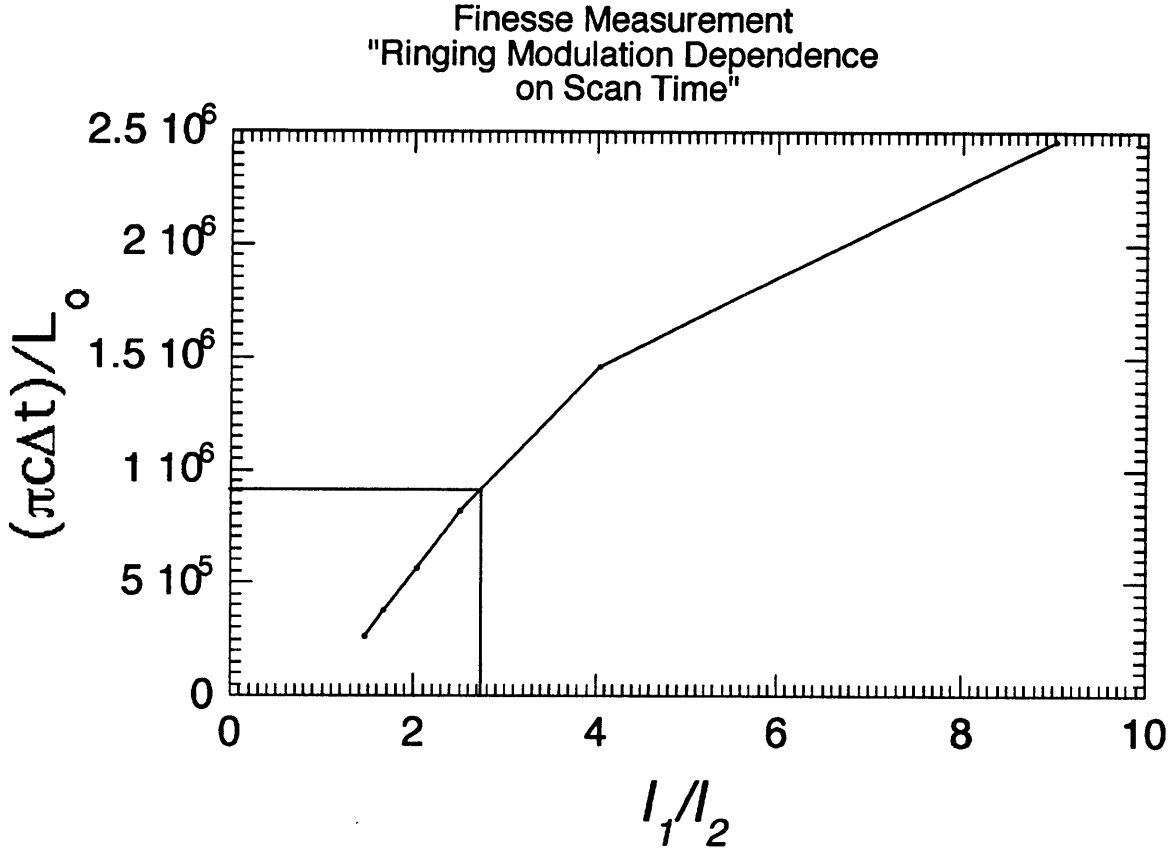

Figure 4-7: Finesse measurement from ringdown modulation, F=910,000. Larger I_1/I_2 represents slower scan speeds.

Chapter 5

The Transmission Coefficient

5.1 Transmission Theory

There are a variety of techniques for measuring the transmission coefficient of the super cavity mirrors. The first technique is to directly measure T for an individual mirror while three other techniques utilize the properties of optical resonators in order to extract the geometric mean of T for the two cavity mirrors. We title the three cavity techniques as (1) reflection on/off resonance, (2) throughput with locked cavity, and (3) ringdown-modified throughput. I discuss the first and the second techniques for breadth of understanding, but I utilize the third, the ringdown-modified throughput technique, and make verification with the direct measurement of an individual mirror.

5.1.1 Transmission of Individual Mirror

On the surface, this seems like a simple measurement. Apply a known incident power, measure the transmitted power, then divide the transmitted by the incident to get the value for transmission. It is not quite that easy since the typical transmission for super cavity mirrors is extremely low. Measurements of such low transmission depend on angle of incidence, spot size, spectral purity of the incident beam, as well as a number of experimental shielding precautions to prevent stray photons from skewing the measurement. Under these conditions, the transmission is extremely

sensitive to the incident angle. Consider an angle of incident of just 1 degree. In just the first thin film the optical path length for perfect quarter wave thickness is changed by a factor of 3.45×10^{-5}. While this appears to be negligibly small, it will change the value of the sine squared term by .3% in Eq. (3.15). With R near unity, this change can substantially reduce the transmission in that particular thin film. The other more important impact is that R is also reduced for non-normal incidence, thus tremendously increasing what is transmitted at the opposite end of the mirror.

Spot size also has its impact on the transmission measurement. Due to the mirror radius of curvature, the geometry of a larger spot size then creates slight non-normal incidence. Additionally, thin films are known to have localized defects [16], and the larger the spot size, the greater statistical chance of encountering a defect. In addition, because the mirrors are reflective in a region of wavelengths, the measurement of T also depends on the spectral purity of the incident beam. Consider the mirror as a filter for the designed wavelength while light far from the design wavelength then sees the mirror as a transparent object. Even lasers locked to a specific wavelength can exhibit background fluorescence from the laser gain medium at other wavelengths such that the measured T is generally at the upper limit. Finally, stray light becomes substantial in the measurement of transmission on the order of parts per million. Ten milliwatts incident power would only amount to transmission of 10 nW. This does not seem to pose a major problem, but experimentally I will show that even scatter from table mirrors can contaminate such a measurement.

So this seemingly simple measurement can pose some experimental difficulties. Some precaution are to (1) align the incident beam with the reflected beam in order to guarantee normal incidence, (2) focus the incident beam to the size of the resonator spot size, (3) filter the incident beam with an interference filter, which removes the fluorescence background, and (4) design the experiment such that all potential scattering optics are distant from the measurement, which must be heavily shielded. Still, the advantage of this technique is that the measurement is for a single mirror rather than the geometric mean of two cavity mirrors.

5.1.2 Reflection on/off Resonance

Consider the discussion of the Fabry-Perot etalon in Chapter 3. Recall Eq. (3.14)

$$\frac{I_r}{I_i} = \frac{4R\sin^2(\frac{\delta}{2})}{(1-R)^2 + 4R\sin^2(\frac{\delta}{2})} .$$

We define resonance when δ is an integer multiple of 2π. The values for I_r/I_i can then be expressed for the on and off resonant conditions.

$$\frac{I_r}{I_i} \approx \left(\frac{L'}{1-R}\right)^2 \quad \text{on resonance} \tag{5.1}$$

$$\frac{I_r}{I_i} \approx 1 - L' \approx 1 \quad \text{off resonance} \tag{5.2}$$

Then the ratio of reflection on and off resonance β_R becomes

$$\beta_R \approx \left(\frac{L'}{1-R}\right)^2 \tag{5.3}$$

A finesse measurement leads to values for $1 - R$, which in turn determines $T + L'$. The measurement of β_R then determines T and L' from Eq. (5.3).

5.1.3 Throughput with Locked Cavity

This is a particularly delicate measurement to make due to the physical stability problems that can be encountered with the cavity. Without cavity locking, the SAL cavity has a 50 kHz frequency jitter and the resonant frequency drifts slowly but predictably at a rate of about 1 MHz/sec even if shielded from a sudden perturbation such as that caused by PZT stress or changes in vacuum presure or temperature. Details of the locking proceedure are found elsewhere [1]. The locking is performed using a technique referred as the cavity-side-lock method. In this case, the difference between the cavity signal and a reference signal is delivered to a differential amplifier which then creates an error signal which is then fed back to the length-controling PZT. This procedure also requires the stabilization of the probe since it is used as

both the reference signal and the cavity signal. Therefore, the probe laser is stabilized using an FM spectroscopy stabilization process [17].

The cavity is locked to the resonance with the stabilized pump laser beam. Then, a steady state cavity output is achieved once the cavity field has built up. This output is detected using an avalanche photo diode, the details of which are described in the next section. As a result, the direct measurement of throughput is achieved with the measurement of the cavity input and output powers. In earlier experiments, this technique was used to measure throughput. Along with the finesse measurement which specifies $1 - R$, and hence $T + L'$, the throughput $\mathcal{T}$ then leads to the value of T using

$$\mathcal{T} = \frac{I_{out}}{I_{in}} = (\frac{T}{T + L'})^2 . \tag{5.4}$$

Furthermore, this calculation for T, then allows for the calculation for L'.

For example, in early SAL experiments, the finesse was $7.9 \pm 0.1 \times 10^5$ and the measured throughput was $(7.9 \pm 0.4) \times 10^{-2}$ which leads to $T = 1.1 \pm 0.1$ ppm and consequently $L' = 2.9 \pm 0.1$ ppm [1].

A precautionary comment is necessary regarding the incident power. Because this is a steady state build up on the cavity field, the cavity is held at resonance as opposed to sweeping across resonance in the ringdown measurements. This creates a prolonged intense internal cavity field about 1 million times greater than the incident power. The potential result is heating of the mirror surfaces. This will generate instabilities thus making the locking procedure more difficult. Or even worse with more intense incident powers, there is likelihood of irreversible laser induced damage (LID) of the mirror surface. Therefore, the incident power should be kept very low, typically less than a microwatt for this measurement. While the LID has not been studied in this research, the instabilities created from surface heating is the topic of of the next chapter concerning the measurement of absorption.

5.1.4 Ringdown-Modified Throughput

In this technique we utilize our knowledge of the magnitude of the build-up of the cavity field in a quickly scanned cavity. Under this condition, the cavity transmission is reduced because the cavity field is not allowed to grow to its full capacity. This is because the scanned cavity crosses over resonance in such a short period of time (a few nanoseconds). From the ringdown formalism of Chapter 4, we can express a time-dependent throughput as the following

$$\mathcal{T} = \frac{I_{out}}{I_{in}} = T^2 R^{2l} \left| \sum_{n=-l}^{\infty} r^{2n} exp\left[-ikv(\frac{2L_0}{c})n^2\right] \right|^2 \tag{5.5}$$

where l is defined by $t = \frac{2L_0}{c} l$. This then shows the time dependence of the above expression.

This equation for throughput demonstrates the cavity output dependence on both the scan velocity v and the exponential decay of the internal field with increasing number of round trips l. Note that when the velocity goes to zero, the cavity output is then allowed to reach a maximum followed by a field decay defined as the cavity decay time. However, for non-zero values of v, the output is further reduced due to the ringdown of the cavity. It is the aim of this analysis to analytically determine this additional reduction factor in the cavity output. As a result, we can determine the value for T. The experimental measurement of throughput and the calculation of the throughput reduction factor is necessary to determine T. This reduction is further discussed below.

Now let's interpret the ringdown modified throughput. The throughput is proportional to T^2. For simplicity, we introduce the parameter $\beta^2 = \frac{4\pi v L_0}{\lambda c}$. Then we can write

$$\mathcal{T}(l) = T^2 R^{2l} \left| \sum_{n=-l}^{\infty} r^{2n} \exp\left[-i\beta^2 n^2\right] \right|^2 \tag{5.6}$$

If we take the first three terms of this summation, a recursion relationship can be

established: $S_l = r^2 S_{l-1} + e^{i\beta^2 l^2}$. And so we can express throughput as the following

$$\mathcal{T}(l) = T^2 |S_l|^2. \tag{5.7}$$

This formalism can be run in a program with the input variables transmission coefficient T, finesse F, scan velocity v, and cavity length L_0. Over time (increasing l) the throughput exhibits the characteristic ringing. Consider a given cavity with length L_0, F, and T. As we vary the cavity scan speed, we can generate a plot of throughput versus scan speed for a given cavity. As demonstrated in Figure 5-5, the curve shows the relationship between mirror velocity and throughput for a cavity with finesse of 1 million and T=1 ppm.

5.2 Measurement of T

As discussed above, there are a few means of measuring the transmission coefficent. Here I report data for measuring T using the direct incidence and the ringdown modified tehcniques. This section is broken into subsection for the direct measurement, the avalanche photo diode, and the ringdown modified throughput.

5.2.1 Direct measurement of T

In this work, I made measurements of T using either a power meter or an avalanche photo diode. Both measurements are susceptible to background noise because the transmitted beam is often at nW levels. Extreme care was needed in shielding the detector in this measurement. As will be discussed in the measurement of S, the integrating sphere afforded an ideal setup for measuring T directly because of the shielding it can provide to the detector, see Figure 5-1. Prior to introducing the mirror sample to the setup, the incident laser beam was aligned so that it passed through a 2 mm aperature at the entrance of the integrating sphere and exited the other side of the sphere at its circular port.

The mirror sample was placed in the path of this laser beam, which was further

focused onto the mirror with a lens (f=30 cm). The result is a faint transmitted laser beam that retraces the original beam into and out of the integrating sphere. Minor alignment was done with two table mirrors (R=99%) and observed with an IR viewer. The result was that the transmitted beam reflected off of the two mirrors and then traveled appoximately 0.5 m to the integrating sphere where it entered and exited without contact.

This condition was verified using of the PMT photon counting system of the integrating sphere. The check was made by photon counting with both the entrance and exit ports open under the condition of either a blocked or unblocked transmission beam. There was no difference between the two conditions, thus verfying that the transmitted beam is entering and exiting without clipping the aperatures of the sphere. A further verification that the transmitted light was entering the sphere was made by blocking the exit port. The PMT signal changed from 3,000 cps to 10,000,000 cps, thus verifying the entrance of the transmitted beam.

Another step to an accurate measurement was to insure that no additional stray light entered the sphere. This was carefully done with the use of aperatures along the beam path and with a shielding pipe along part of the beam path. As a result, the transmission was determined by measuring the incident power before the mirror and the power at the exit port of the integrating sphere. Incident power was measured with a Coherent Power Meter model 210 and the power at the exit was measured with a Newport Research Power Meter model 815. Care was taken to calibrate the two power meters for this measurement. The Coherent power meter was calibrated for the visible and has a power reduction of 15% at 791 nm. The Newport power meter has a wavelength calibration setting that was set to the appropriate level for 791 nm. The measured transmission for a given mirror was typically 0.6 ± 0.2 ppm which was within the 0.5 ppm design specification of the manufacturer.

In the other T measurement, the Newport power meter was replaced with an avalanche photo diode. In this measurement, a resonator was built and the incident laser beam was focused to the TEM_{00} mode. The APD was used to measure the cavity transmission. Consequently, it served to observe the alignment of the TEM_{00}

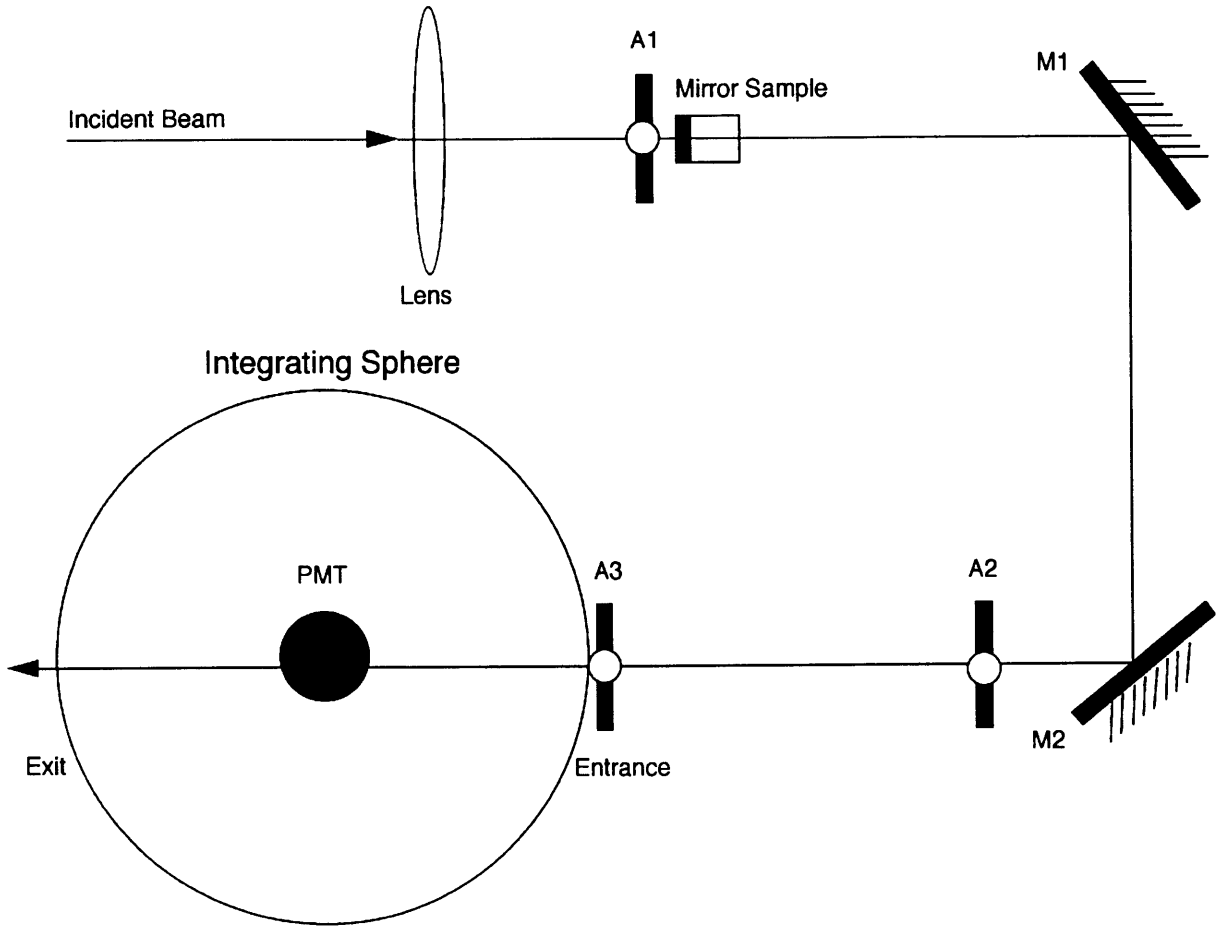

Figure 5-1: Configuration for T measurement using integrating sphere. A1, A2 and A3 represent aperatures, and M1 and M2 are alignment mirrors.

mode as well as alignment of the transmitted beam. Once the cavity was built and the laser was aligned, the front mirror of the cavity was removed, leaving a focused laser beam incident on a mirror with the transmission well aligned with the APD. The output of the APD was sent to an oscilloscope to measure the voltage. The next step was to calibrate the voltage to an incident power. For calibration, CW light was incident directly onto the APD. This was done by attenuating the laser to nanowatt levels with neutral density filters, and measuring the corresponding voltage. Then with the incident power determined by the Coherent power meter, and the transmitted power determined by the calibrated APD signal, one can determine the transmission of a particular mirror. This measurement resulted in an initial value of T=1.0 ppm. However, due to linearity concerns in the APD response, this technique was abandoned in favor of the techniques without the APD.

5.2.2 The Avalanche PhotoDiode

The precise knowledge of the APD characteristics was neccesary to conduct the cavity ringdown modified throughput measurement since the measurement depends on the APD responsivity. I operated the APD in the current mode such that detected signal is proportional to the current generated by the APD. The experimental setup was identical to that used in the ringdown finesse measurement in Chapter 4. The difference here is that instead of having temporal interest in the decay of the cavity field, I was interested in the amplitude of the cavity output.

Then the measurement is fairly straightforward. Measure the current, apply a conversion factor of the current to incident intensity, and calculate the incident intensity at the APD. I measure the current by measuring the voltage across a known terminal resistor. For this measurement, I use a LeCroy digital oscilloscope model 9310M Dual 300 MHz with an internal impedance of 1 MΩ. The detector circuit also has an impedance of 1 MΩ. So if I measure the voltage across a terminal resistor, the effective resistance seen by the oscillscope is all three resistors in parallel. Clearly the dominant term is the smallest terminal resistor.

The conversion factor relates the current generated to the incident intensity. This

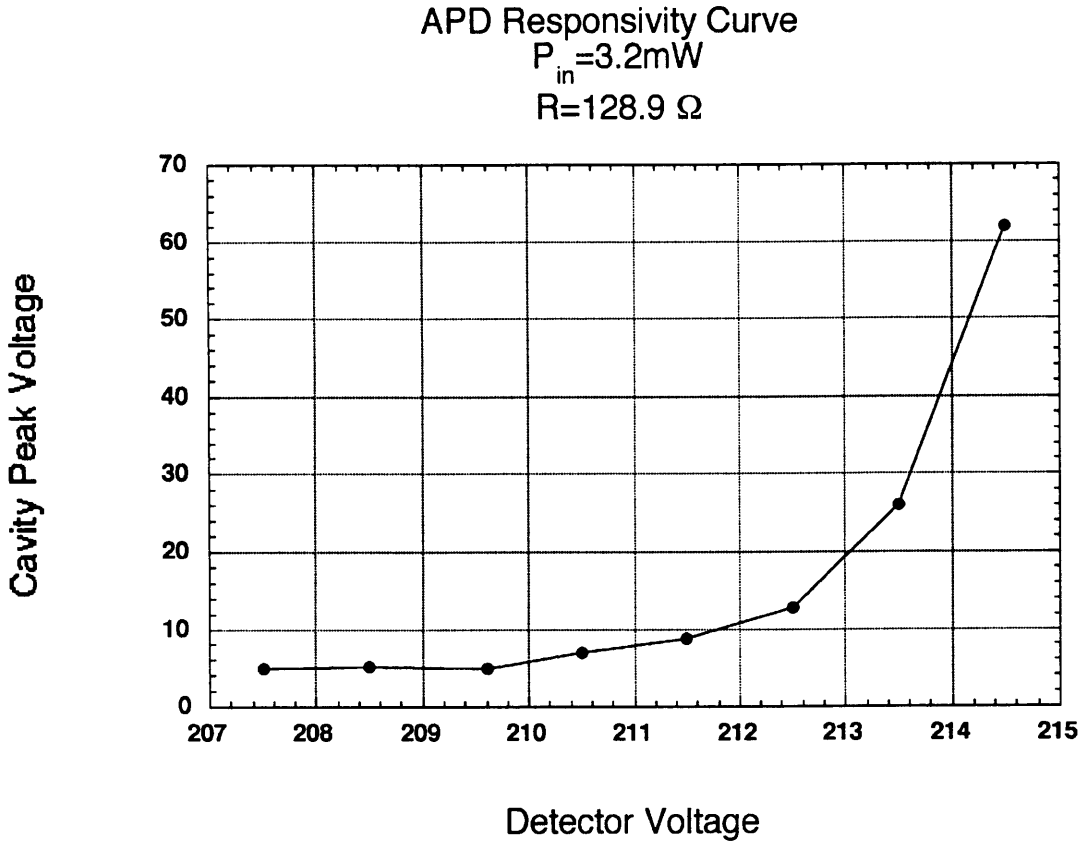

Figure 5-2: APD sensitivity to operating voltage. Plot of cavity output while varying operating voltage. Suggested operating voltage is -209.6 Volts and breakdown voltage is -214.8 Volts.

is defined in a quantity called the APD "responsivity" which is in units of amperes per watt. This can be a somewhat elusive quantity as we have found that responsivity depends on (1) the externally applied bias or operating voltage, (2) the current impedance, and (3) the incident power. In general, higher responsivity is found at higher operating voltages, lower current impedance, or lower incident power.

In the operation of the APD, two externally applied voltages are important. The breakdown voltage is the threshold for operating the APD in a photon-counting mode. In this mode, the APD can respond to individual photons, hence establishing a very sensitive but noise susceptible detection scheme.

The operating voltage is the bias used to operate the APD in the current mode. The manufacturer's operating voltage is the externally applied voltage that allows for the avalanche amplification process and that also achieves the manufacturer's prescribed responsivity. This operating voltage is set by "flooding" the entire APD

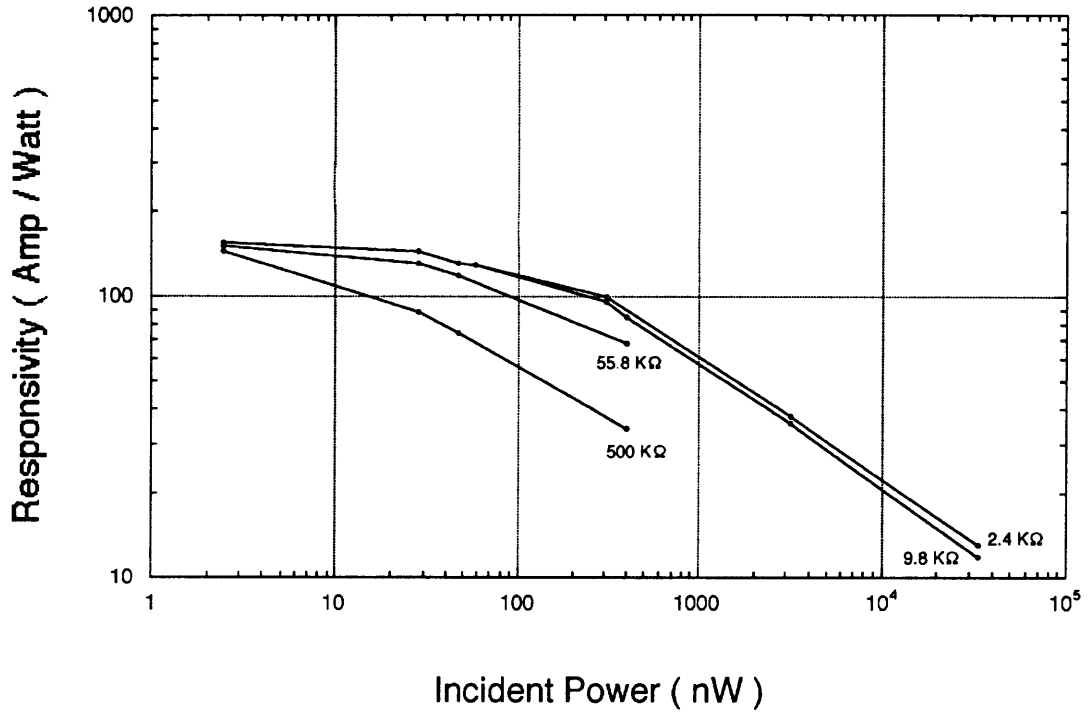

Figure 5-3: APD responsivity. Power varied from 2 nW to 50 μW and impedance varied from 2.4 KΩ to 500 KΩ.

detector face with a known power of CW laser light at a wavelength of 830 nm. The manufacturer then increases the applied voltage until the desired responsivity is achieved. This voltage is then defined as that particular APD's operating voltage. The APD responsivity is very sensitive to changes in the operating voltage as seen in Figure 5-2 where the peak voltage from the cavity transmission is plotted against applied voltage. Notice that in the region below the prescribed operating voltage the APD is characteristic of an ordinary photo diode and as the voltage is increased above the operating voltage the responsivity increases due to the effects of the avalanche process.

Since the precise value for the responsivity is needed to determine T using the ringdown-modified technique, a variety of tests were performed on the APD. As with the manufacterer's procedures for setting the operating voltage, I applied a known 791 nm CW laser beam to the APD detection face and measured the responsivity. The difference was instead of flooding the detector face, I focused the beam to a

spot size comparable to the cavity transmission. Representative data for APD serial 1291 at an operating voltage of -212.5 V is shown in Figure 5-3. In this log-log plot, the flat region represents a linear/constant region of responsivity and the straight sloped region represents detector saturation where the responsivity is power dependent. Under these conditions the APD experiences saturation at around 100 nW. In the region below saturation, the responsivity was determined to be 150 A/W. This was slightly higher that the manufacturer's responsivity of 128 A/W. However, the actual operating voltage was higher than suggested but well below breakdown.

The situation can be problematic for incident powers higher than saturation. Still this problem can be minimized by the fact that the APD response is well behaved. So if the data is for a given terminal resistor and operating voltage, we can replicate the conditions during our transmission measurement with confidence about the responsivity. For a 120 Ω resistor, the fit data follows the emperical fit

$$\mathrm{Resp_{fit}} = (.15064)\mathrm{P_{inc}}^{-0.438} .$$

This can be solved simultaneously with the transmission data to find $\mathrm{P_{inc}}$:

$$\frac{\frac{\mathrm{V_{osc}}}{\mathrm{R_{eff}}}}{\mathrm{P_{inc}}} = (.15064)\mathrm{P_{inc}}^{-0.438}$$

Solving for $\mathrm{P_{inc}}$ we get

$$\mathrm{P_{inc}} = \left(\frac{\frac{\mathrm{V_{osc}}}{\mathrm{R_{eff}}}}{.15064}\right)^{1.78} \tag{5.8}$$

Here $\mathrm{R_{eff}}$ is the effective resistance of the three impedances discussed above, and $\mathrm{V_{osc}}$ is the voltage measured on the LeCroy osciloscope.

The final step was the determination of whether the APD was saturated during the ringdown measurment of the cavity finesse. The saturation was due to a thermal effect from the change in the APD temperature when exposed to a CW laser beam [18]. So the analysis of whether the APD was saturated can be made with the average incident power. In the case of a scanned, high Q Fabry-Perot, the cavity field can grow to be very intense, but the duration of this transmission is very short compared

to the length of the cavity scan. Under typical conditions, the cavity resonance time is about 10 ns, while the cavity scan is 10 ms. This suggests a very small incident power if averaged over the length of the scan. Even with modest approximations of throughput for a typical incident power of 10 mW, the corresponding average power on the APD would be just 10 nw. This is well below the saturation region and then leads to the use of 150 A/W for the responsivity. This was confirmed experimentally by verfying that the signal size changes linearly with the input power at the power level that is typically used in the ringdown measurement.

5.2.3 Ringdown Modified Throughput

Figure 5-6 shows the ringdown cavity output for a scan corresponding to a mirror velocity of 13.0 μm/s and finesse of 900,000. Using a responsivity of 150 A/W, P_{inc} is calculated to be 1.841 μW. The cavity input power was 3.2 mW so that the ringdown throughput was measured to be 5.75×10^{-4}. This, of course, was the modified throughput which was reduced by the fast cavity scan.

In Figure 5-4, the theoretical throughput modulation is plotted for the SAL cavity with assumed value of T=1 ppm and actual values of mirror velocity 13.0 μ m/s and a finesse of 900,000. Recall that the measured throughput was 5.75×10^{-4} and the theoretical throughput corresponds to 2.248×10^{-3}. Then, noting that $\mathcal{T} \propto T^2$, the scaling equation would be

$$T = \sqrt{\frac{5.75 \times 10^{-4}}{2.248 \times 10^{-3}}} \times 1\text{ppm}$$

The result is then $T = 0.51 \pm 0.01$ ppm.

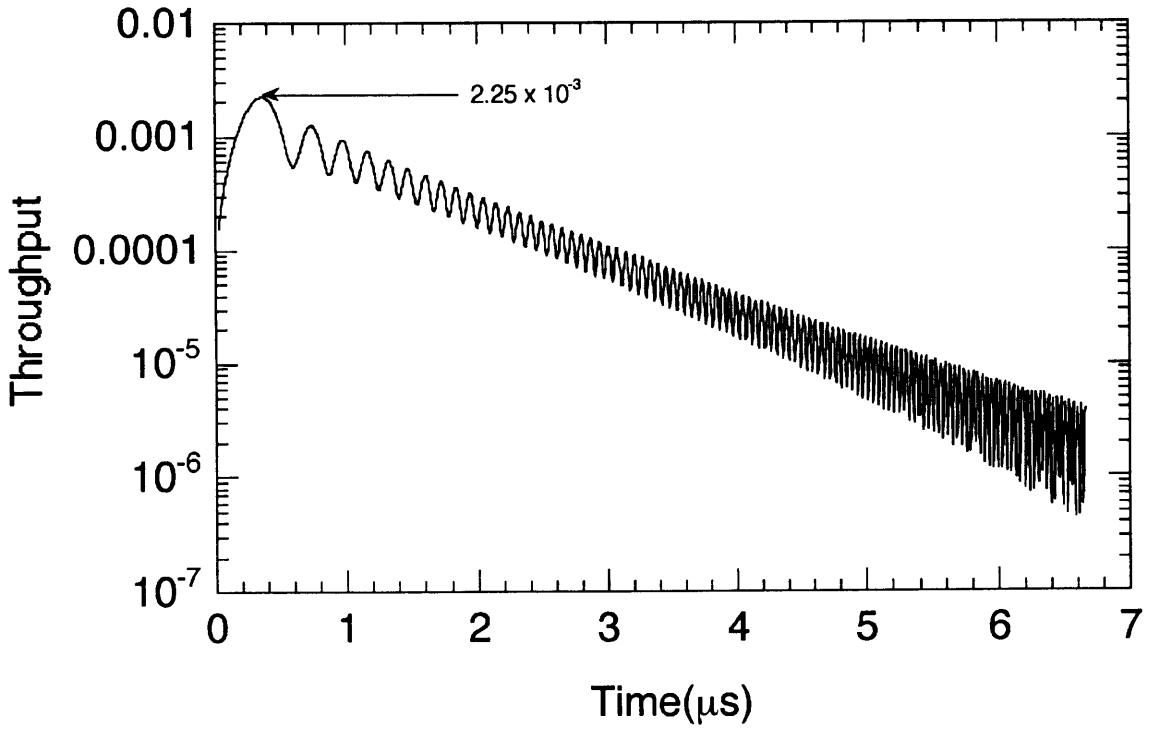

Figure 5-4: Theoretical Throughput for F=9 $\times 10^5$, v=13 μm/s, and $\mathcal{T}$=2.24 x 10^{-3}.

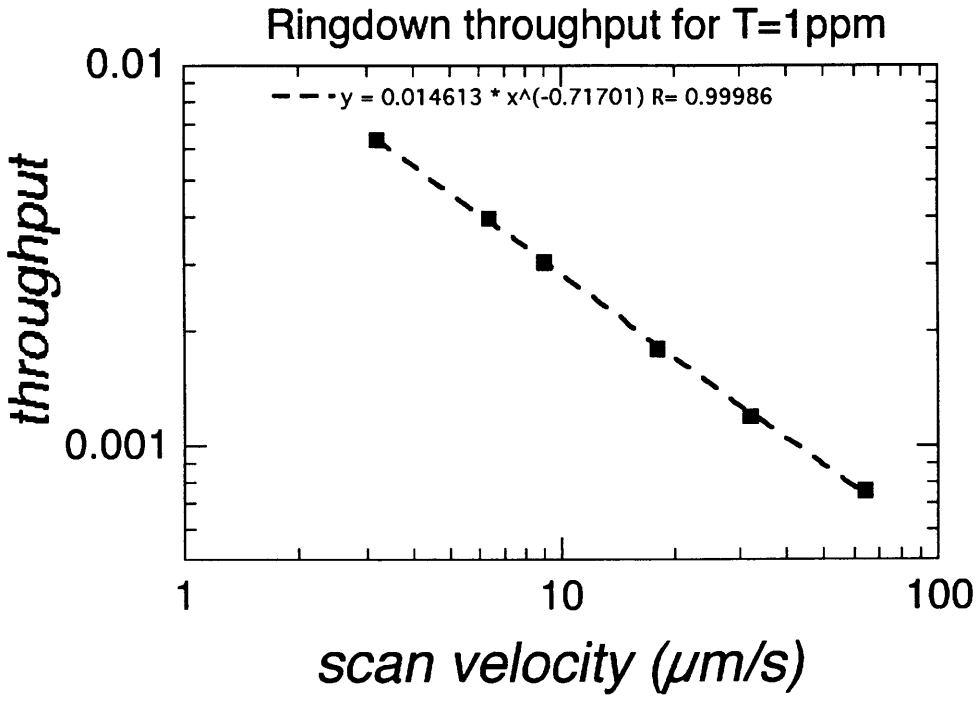

Figure 5-5: Ringdown modified throughput for assumed 1 ppm transmission and F=1 million.

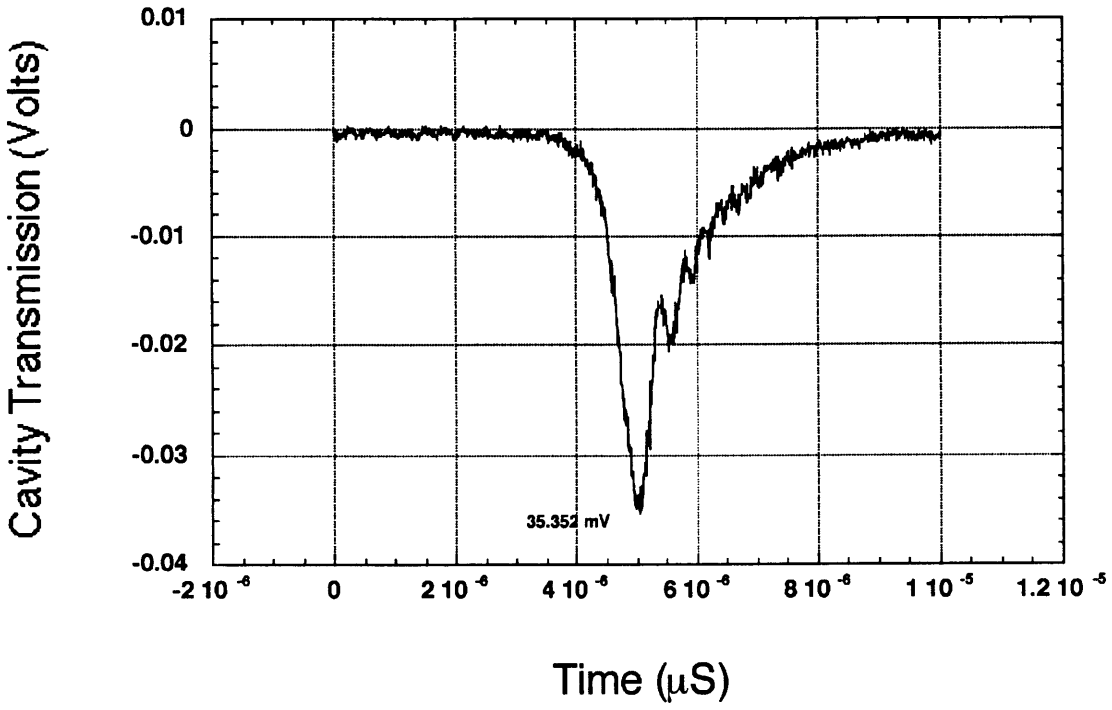

Figure 5-6: Cavity Transmission. P_{in}=3.2 mW, R=128 Ω, V_{osc}=35.352 mV, v=13 μm/s.

Chapter 6

The Absorption Coefficient

This chapter discusses the absorption theory, which also includes an overview of the literature regarding thermal characteristics of thin films and recent advances in the measurement of these characteristics. This is followed by the theory for the absorption induced optical bistability and the measurement of absorption.

6.1 Thin Film Absorption

Measurements of R and T allow the determination of the sum of absorption and scattering. As a result, the upper limit for absorption losses can be estimated. For example, a cavity with finesse of 1 million and mirror transmission of 0.5 ppm then would have a total loss of 2.64 ppm. For a moment, let's assume no scattering so that the upper limit of absorption is 2.64 ppm.

6.1.1 Thin Film Heating

The fundamental effect of energy absorption is heating. So one approach for measuring this absorption is to measure the temperature change of the heated material. Is this feasible at our upper limit of absorption? Considering some rough numbers, heating generated from a 1 KV incident beam in vacuum would generate only a change of temperature in the range of nano-degrees celcius for an object comparable to our mirrors. This would be difficult to measure with the performance of any

existing thermocouples.

Another device that has been widely accepted as a means of measuring the the thermal properties of thin films is the thermal comparator [19]. As a tool for those interested in the laser induced damage (LID) of optical materials, the thermal comparator offers answers to the specific problem of heat transfer in thin films. It operates with physical contact at the mirror surface under a given pressure and applied temperature while a thermocouple monitors the transfer of heat to the mirror. This does not provide information about the optical absorption qualities of the thin films, but it is our source for information concerning the thermal properties of thin films. As widely noted in literature regarding LID, thin films have lowered thermal conductivity than their parent bulk materials [20]. This is attributed to the microstructure of the thin films and a proposed thermal resistance between thin film layers. Consequently, thin films are less capable of diffusing heat, and damage is observed at lower levels than expected. What must be taken from this discussion is the need to use modified values for the thermal conductivity of thin films.

6.1.2 Photothermal Deflection Spectroscopy

The absorption and subsequent heating of thin films has been the subject of a relatively new field termed photo-thermal deflection spectroscopy (PDS). PDS provides a relative measurement of absorption to sub-ppm levels [5]. These measurement techniques rest on the assumption of thin film bulging and film index of refraction changes due to temperature changes. These techniques typically employ a modulated laser beam to generate thermal waves that are subsequently detected and analyzed to gather information about the sample [5]. The early configuration of such experiments used two laser beams, one as a pump beam to heat the mirror surface, and the other as a probe beam to examine its spatial deflection while transmitted through the heated mirror [21]. Because the heat deposited on the mirror surface results from absorption in the thin films, the temperature distribution in the mirror is proportional to absorption. In the most common case of the thin films being thermally thin, we then consider the heat dissipation of the mirror system to be equivalent to the dissipation

in the mirror substrate. If the pump beam is chopped, the temperature distribution can take on two extremes for either high or low frequency chopping. In both cases, the result is a deflection that is proportional to absorption A. By measuring this deflection angle, one can determine the absorption coefficient of a particular mirror.

In more recent applications of these same principles, two additional configurations for this measurement have evolved. In the mirage configuration, the probe beam is incident parallel to the mirror surface and contact with a "bulged" mirror surface then displaces the probe beam [16]. The reflection configuration orients the probe beam nearly normal to the surface and the reflected beams is then analyzed [22].

The power of the PDS is that it is a precise relative absorption measurement owing to levels of ppm; it offers measured values for the thermal conductivity of thin films; and perhaps most important to our investigations, it demonstrates localized absorption and provides causes for this absorption [5]. Unfortunately, the ability to measure absolute absorption does not exist without a known absorption sample for which to calibrate the PDS measurements [23].

6.2 Absorption Induced Optical Bistability

The following theory was developed by K. An *et al.* [6]. The absorptive heating can cause thermal expansion. Crude estimates of thermal expansion may only be in the angstrom range. Unlike the undetectable change in temperature, this is a discernible distance for an interferometer. As such, we set out to measure absorption using three principles of physics: thermal diffusion, thermal expansion, and a Lorentzian cavity lineshape.

The three dimensional thermal diffusion equation is given by

$$\frac{\partial \psi}{\partial t} = \frac{\kappa}{s}\Delta^2\psi \tag{6.1}$$

with ψ the temperature, κ the thermal conductivity, and s the specific heat (per unit volume) of the mirror (the thin film/substrate system). In the case of the mirrors

in the SAL cavity in vacuum (see Figure 2-2), heat dissipation occurs only at the bottom surface of the mirror and flows into a heat resevoir at a fixed temperature of ψ_0. The heat transfer is conserved, giving rise to a reduction of the heat flux roughly by the area ratio $(r/w)^2$ as we get further away from the heated area.

Let us model the mirror substrate under the conditions of finite length Z and infinite radius R. Now apply a Gaussian laser beam with intensity mode waist w, with $w \ll R, Z$. Then the length change due to thermal expansion of the mirror substrate is given by:

$$\Delta Z = C_{ex} \int_0^Z \psi(\vec{r}) dz = (C_{ex} C_0 P_i A)/(\kappa\pi) \tag{6.2}$$

where C_{ex} is the thermal expansion coefficient of the substrate, P_i is the incident power, and C_0 a constant near unity determined by the geometry of the mirror such that

$$C_0 = \frac{1}{2} \int_0^\infty dy \, e^{-\epsilon^2 y^2/4} \frac{\cosh y - 1}{y \cosh y} \tag{6.3}$$

with $\epsilon \equiv w/Z \ll 1$ with w the spot size and Z the height of the mirror. The solution to the thermal diffusion equation can be written as

$$\psi(\vec{r}) = \psi_0 + T_0 \int_0^\infty dy \frac{J_0(y\rho/w) e^{-y^2/4} \sinh y(1/\epsilon - z/w)}{\cosh y/\epsilon} \tag{6.4}$$

where $T_0 = \frac{P_i A}{2\pi w \kappa}$ and J_0 is the zero order Bessel Function.

6.2.1 Thermal Expansion in the Mirrors of a Fabry-Perot Resonator

Consider a Fabry-Perot resonator with the distance between the mirror bottom ends held fixed. Then the power of each traveling wave component inside the cavity is expressed

$$P_i = P_0 \frac{T}{(1-R)^2} \mathcal{L}(\omega), \tag{6.5}$$

where P_0 is the incident probe laser power and $\mathcal{L}(\omega)$ is the lineshape function of the cavity with ω the frequency of the laser beam. Under conditions of no thermal expansion in the mirrors, the lineshape function is Lorentzian:

$$\mathcal{L}(\omega) = \frac{1}{1 + (\frac{\omega - \omega_c}{\gamma_c})^2} = \frac{1}{1 + x^2} \equiv y_0(x) \tag{6.6}$$

with ω_c and γ_c the cavity resonance frequency and linewidth (halfwidth), respectively. $y_0(x)$ then defines the cavity lineshape function as a function of $x = \frac{\omega - \omega_c}{\gamma_c}$. Thermal expansion of the mirrors effectively reduces the cavity length l so that if the expansion in one mirror is ΔZ, then the cavity length is reduced by $2\Delta Z$. This results in a change in the cavity resonance frequency of $\Delta\omega_c$,

$$\Delta\omega_c = 2\omega_c \Delta Z / L = \frac{2\omega_c C_{ex} C_0 A P_i}{\pi \kappa L} = \left[\frac{2\omega_c C_{ex} C_0 T A P_0}{\pi\kappa(1-R)^2 L}\right] \mathcal{L}(\omega) \tag{6.7}$$

The corresponding change in the lineshape is determined by replacing ω_c in Eq. (6.6) with $\omega_c + \Delta\omega_c$. We can write

$$\frac{1}{\mathcal{L}(\omega)} = 1 + \left\{\frac{\omega - \omega_c}{\gamma_c} - \left[\frac{2\omega_c C_{ex} C_0 T A P_0}{\pi\kappa(1-R)^2 L \gamma_c}\right] \mathcal{L}(\omega)\right\}^2 \tag{6.8}$$

or equivalently,

$$\frac{1}{y(x)} = 1 + (x - \beta y)^2 \tag{6.9}$$

where

$$\beta \equiv \frac{2\omega_c C_{ex} C_0 T A P_0}{\gamma_c \pi \kappa (1-R)^2 L} = \frac{8 C_{ex} C_0 T A P_0 F^3}{\kappa \pi^3 \lambda}\,, \tag{6.10}$$

and we use the following relations: $F = \pi/(1-R)$ for cavity finesse and $\omega_c = 2\pi\nu_c = 2\pi c/\lambda$ for the cavity resonance frequency. The value for β then determines the magnitude of the shift created from the thermal expansion of the mirrors. As β goes to zero, the original, undistorted lineshape is recovered. Let's define a critical incident power P_c such that the β parameter determines an appreciable distortion of

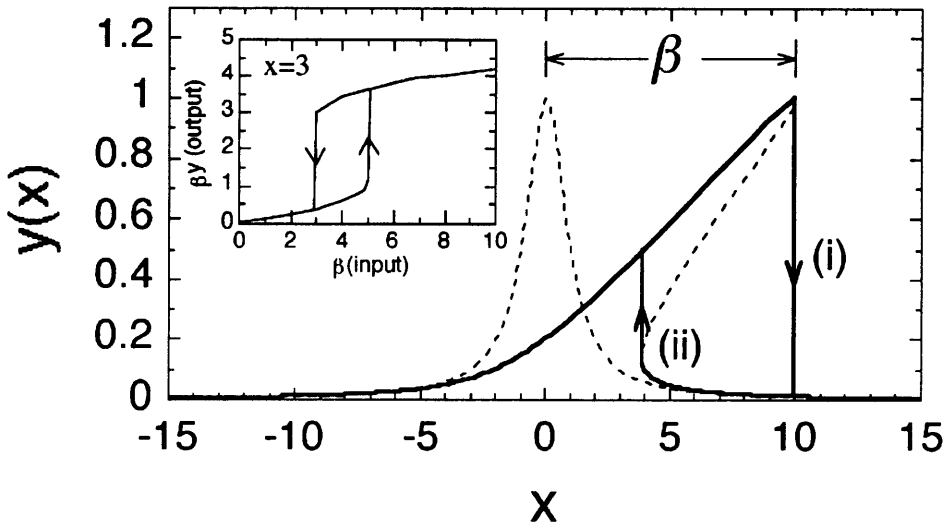

Figure 6-1: Graphical solution to Eq. (6.9).

the lineshape. Define this critical power such that $\beta \equiv P_0/P_c$, then P_c follows as

$$P_c = \frac{\kappa \pi^3 \lambda}{8 C_{ex} C_0 T A F^3} \tag{6.11}$$

The resulting lineshape of this Fabry-Perot is obtained by tilting the Lorentzian $y_0(x)$ as seen in Figure 6-1. Graphically, it can be seen that the solution of $y(x)$ can take on three values depending on the direction in which the variable x changes. Hence, optical bistability arises. As discussed in Reference [6], for a given cavity detuning, two stable transmission states exist depending on the cavity scan direction. From Figure 6-1 path (i) represents an expanding cavity. Along this path, the cavity transmission increases to a peak value of y=1, which occurs at x=β, then drops abruptly to nearly zero. Conversely, when the cavity is contracting, the observed linewidth, depicted along path (ii), is much narrower and the peak value is much smaller than unity. The inset shows the typical hysteresis plot of output power vs. input power which is also a solution for $y(x)$.

6.2.2 Scanned Fabry-Perot

Consider the case where the cavity is scanned. Since the resonance frequency is constantly changing, some different conditions exist from the Fabry-Perot discussed earlier. First, this is no longer a steady state problem because a heating time τ is included for the mirror to reach an equilibrium temperature. Second, because of the heating time, the thermal expansion is dependent on the time integral of the power rather than simply the incident power. Third, this heating time then requires the introduction of the thermal response function $f(t/\tau)$ which is given by [6]

$$f(t/\tau) = \int_0^\infty dq\, q\, \exp(-q^2/4) \sum_{n=0}^{\infty} \frac{(-1)^n}{\phi_n} \exp[-C_0(q^2 + \phi_n^2\epsilon^2)t/\tau] \,, \tag{6.12}$$

where

$$\tau = \frac{C_0 s w^2}{\kappa} \,, \tag{6.13}$$

and

$$\phi_n = \pi(n + 1/2) \,, \text{ n= 0,1,2,...} \tag{6.14}$$

If t is converted to x, the corresponding length change can be expressed as

$$\Delta L \propto \int_{-\infty}^{x} y(x\prime) f((x - x\prime)/x_0) dx\prime \,, \tag{6.15}$$

with

$$x_0 = \frac{2\pi c v \tau}{\gamma_c \lambda l} = \frac{\dot{\omega_c}\tau}{\gamma_c} \,, \tag{6.16}$$

where $\dot{\omega_c}$ is the cavity scan speed in radians/sec. The lineshape function $y(x)$ can now be expressed as

$$\frac{1}{y(x)} = 1 + \left[x - \frac{\beta}{x_0} \int_{-\infty}^{x} y(x\prime) f((x - x\prime)/x_0) dx\prime \right]^2 \,. \tag{6.17}$$

The important conclusion is that the lineshape can be completely determined by the two parameters x_0 and β which are characteristic of the cavity scan speed and the absorptive heat dissipation through the mirror substrate, respectively.

6.3 Measurement of Absorption

As discussed earlier, R, T, and A are measured using the same experimental setup. Minor modifications are necessary for the absorption measurement. In this section, I discuss these changes, report the experimental observations, then make the calculation for A.

6.3.1 Experimental Setup Modifications

Absorption is detected under the scheme of a nearly monochromatic laser probe injected into a slowly scanned cavity. These conditions require two modifications to the setup used for the measurement of R and T. The probe beam needs to be further stabilized and the cavity scan speed needs to be further slowed. To accomplish these modifications, I use the SAL FM locking laser stabilization [17] instead of just locking the laser to its reference cavity, and in place of the oscilloscope, I use a function generator to drive the PZT.

These modifications offer many advantages. The FM locking can narrow the probe linewidth to approximately 200 KHz, and compared to the 50 KHz cavity linewidth, this affords improved coupling to the cavity resonant mode. This added stability is increasingly more critical at slower cavity scan speeds where sound waves and other perturbations can create cavity stability problems. Additionally, the FM locking produces resonant sidebands in the cavity transmission. Because these sidebands are produced at the modulation frequency used in the FM locking, they provide a measuring stick in the frequency domain. They are spaced at the modulation frequency. For example, the FM locking system is modulated at 25 MHz; this results in sidebands that are $\pm$ 25 MHz off of the resonant mode.

The function generator used was a Stanford Research Systems model DS345 synthesized function generator. The advantages in using the function generator to drive the PZT are primarily in the w de range of scan frequencies and voltage shapes and amplitudes. The scan frequencies used in this experiment ranged from .001 Hz to 200 Hz. While the function generator could generate a variety of voltage shapes, I used a

saw tooth voltage shape and an amplitude of 1 Volt peak to peak. The positive and negative slopes of the saw tooth voltage allows for the expansion of the cavity during the upward slope and the contraction of the cavity during the downward slope. By doing this in one period, the anamolous lineshape and obvious amplitude differences between the expanding and the contracting cavity are hard to go unnoticed. The voltage of the PZT driver determines the range of cavity length variation. The length variation with only 1 Volt peak to peak is considerably smaller than in the case where the PZT was driven by the oscilloscope's 135 Volts. The advantage in the smaller applied voltage is less unnecessary mirror movement at lengths away from resonance. This again can add stability to an already delicate measurement.

One may ask whether it becomes difficult to find resonance in such a small window. The answer is yes. The solution to this difficulty is to apply an offset voltage to the PZT so that even in the narrow cavity scan range, resonance can be found by simply adjusting the offset voltage. A learned experimental trick is to use two oscilloscopes to monitor the cavity transmission simultaneously.

With the two necessary modifications in place, the absorption experiment could be done. In this investigation, the variables were the scan speed, the incident power, and the terminal resistor across which the transmission signal was measured.

6.3.2 Experimental Observations

The expected outcome of this data is the determination of A. This will be done by fitting theory to the data by adjusting the β and x_0 parameters of Eq. (6.17). However, preliminary observations from this experiment lend justification to the theory that evolved. As a consequence, before getting to the determination of A, it is necessary to highlight some of the important trends in the collected data.

In Figure 6-2, the PZT ramp voltage was superimposed on the plot of the cavity transmission. The ramp voltage that drives the PZT allows the cavity to cross resonance twice during a cycle: once while expanding (positive slope) and once while contracting (negative slope). The notable observation in this plot was the difference in the size and shape of the two resonant lineshapes.

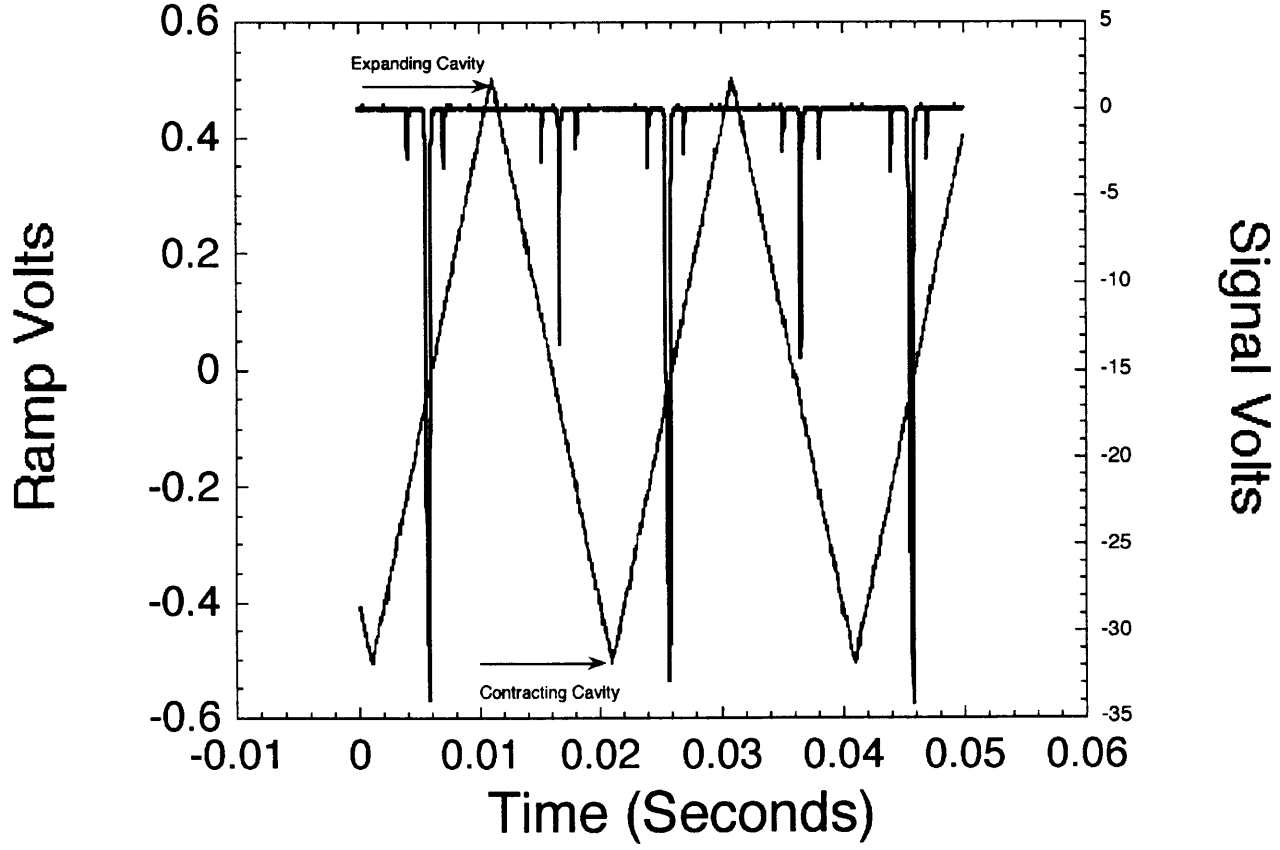

Figure 6-2: PZT ramp voltage superimposed with cavity transmission for P_{in}=5.5 mW at 50 Hz cavity scan.

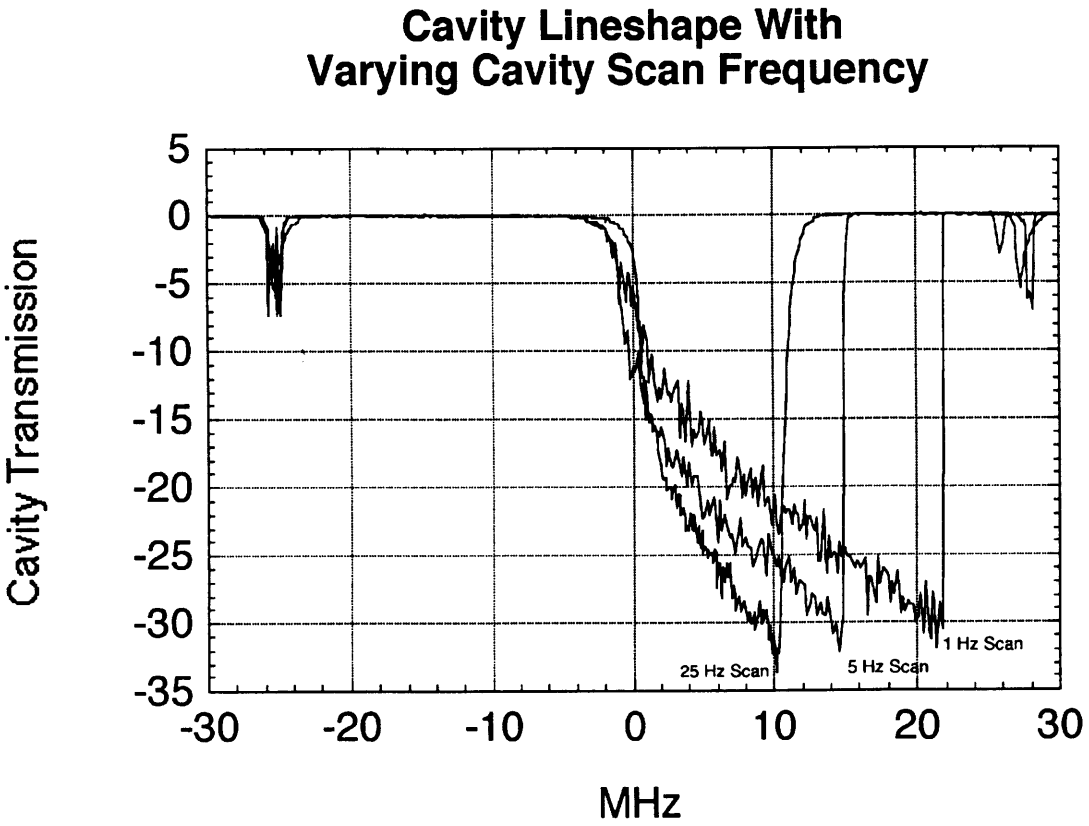

Figure 6-3: Expanding cavity lineshapes for 1, 5, 25 Hz scan.

While the lineshape for the contracting cavity was smaller than that for the expanding, its shape was still Lorentzian. However, the expanding cavity lineshape was far from Lorentzian. As shown in Figure 6-3, the slower the scan, the broader the lineshape. This broadening is subsequently defined as the frequency shift. In the conversion of data in the time domain to the frequency domain, the FM sidebands were used as the yard stick. The separation between the first sideband and resonance was 25 MHz, and this was used in the conversion to the frequency domain. Another observation from this figure is the trend of slightly reduced cavity transmission with slower cavity scans. The opposite would be expected considering optimum pump laser-cavity coupling. This was investigated in this work, and the trend was that there seems to be a temporary, mild degradation of the mirrors with slower cavity scans.

With absorptive heating in mind, the next step was to repeat the slow cavity scans with varying incident power. With scans at 5 Hz, the incident power was varied from 10 mW to .7 μW. The same differences in the two lineshapes appeared at the higher

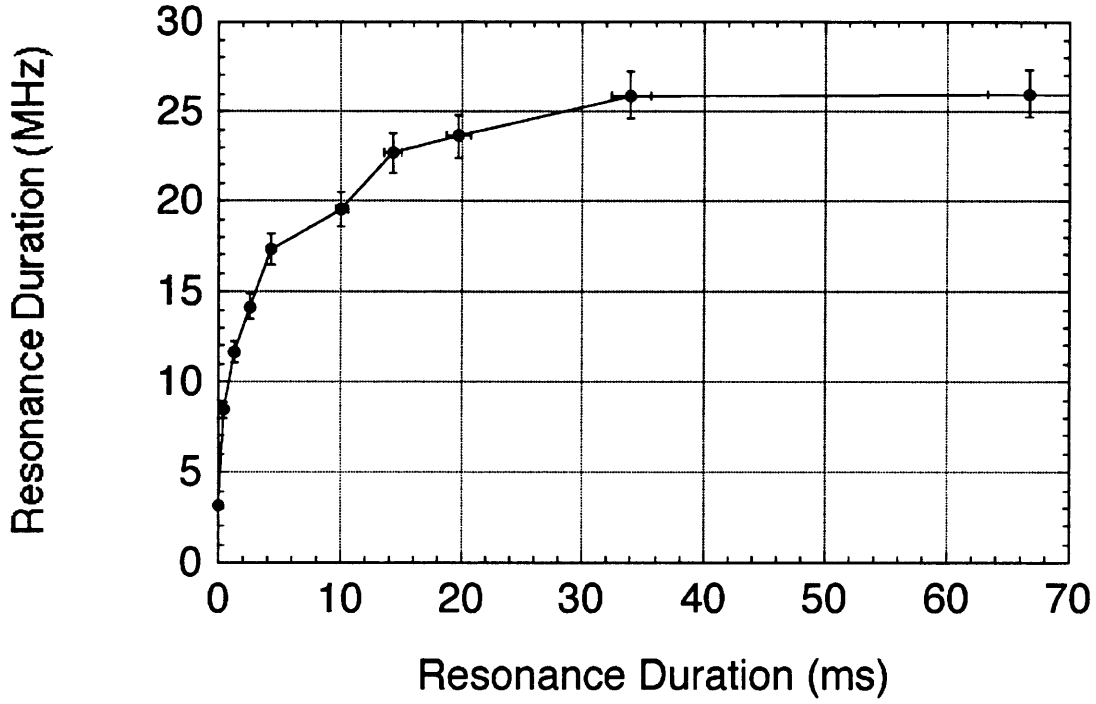

Figure 6-4: Thin film thermal response demonstrated by saturation of frequency shift.

incident powers, but as the incident power decreased, so did the broadening of the expanding cavity. The shape and size of the two lineshapes become more similar at lower powers. In fact, when the incident power reached 0.4 mW, the two lineshapes had no differences. With a finesse of about 1 million, this corresponds to an internal power of .4 kW. It was around this power that I assume absorptive heating starts to affect the mirror thin films.

Of course, the heating of the thin films also depends on the time in which the energy is deposited. A ns-pulse of a 10 kW laser certainly will not have the same deposition of energy as 5 seconds exposure at the same power. In the cavity, the exposure time was analogous to time on resonance, which is a function of scan speed. In Figure 6-4, the graph demonstrates the dependence of heating on the cavity scan speed. With the incident power fixed at 5.5 mW , the cavity scan speed was varied and the observed frequency shift was plotted. This graph clearly demonstrated saturation occurring at around the 35 ms resonance duration. The corresponding cavity scan frequency was 2 Hz. It was this information that inspired our concepts of thin film

heating and steady state heat diffusion.

While the steady state condition was considered for the calculation of absorption, this absorptive heating was clearly a dynamic non-destructive event. As seen in Figure 6-2, in consecutive PZT cycles, the thin film experiences expansion followed by contraction back to its equilibrium state, over and over again. Still there was no degradation in the cavity performance under normal operating conditions. Given the following observations, the following conclusions were made regarding the slow scan anomalous cavity lineshape. First, while absorption in the mirrors was very small, it was detectable in the form of thermal expansion in the mirrors such that this expansion served to prolong the cavity resonance while the cavity was expanding and to curtail the resonance as the heat was dissipated and the cavity contracted. Second, there was a threshold energy at which this absorption presents detectable effects.

6.3.3 Calculation of A

The calculation of A was done with the fitting of theory to the data. Preliminary knowledge of the cavity T is necessary to make this calculation. In this case, we used $T = 0.8 \pm 0.3$, the average of all T measured to that point. As seen in the theory section, the cavity lineshape was viewed in terms of a tilted Lorentzian. As such, for different amounts of tilting a different frequency shift could be fit. In Figure 6-5, the data was fit for two different scan speeds. The inferred absorption from these fit was A=0.3±0.1 ppm. In addition, as seen in Chapter 5, the APD detection scheme can experience saturation at high incident power. This further deforms the observed lineshape in the absorption measurement. As a result, we accounted for this saturation using the power dependent detector responsivity given by Eq. (5.8).

6.3.4 Absorption Connection to Optical Bistability

Optical Absorption is a well known phenomenon in which absorption or dispersion in a medium of a resonator induces an optical path length change proportional to the

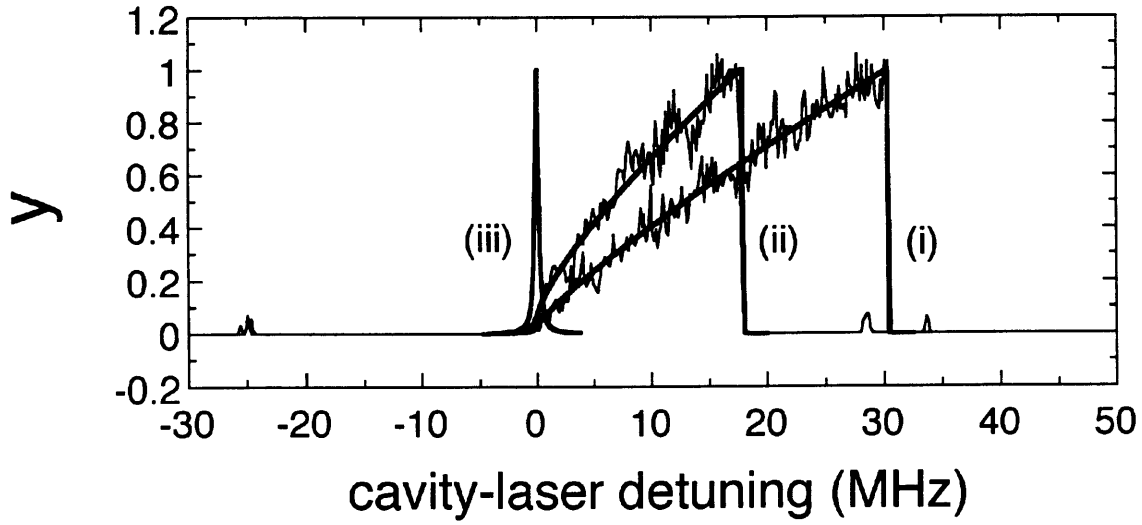

Figure 6-5: Absorption theory fit to data resulting in A=0.3 ppm. Parameters: P_0=10.0 mW, ϵ=0.0075, with cavity scan speed (i) $\dot{\omega_c}$=-0.9 GHz/sec and (ii) $\dot{\omega_c}$= -7.2 GHz/sec. (iii) is unmodified cavity lineshape.

intracavity light intensity in such a way that cavity transmission exhibits more than one stable operating point [6]. Inherent in the description of optical absorption is the optical nonlinearity of the medium. However, there have been numerous reports of this phenomenon in resonators without an intracavity medium. One such example is caused from the radiation pressure exerted by the intracavity field on movable mirrors [24]. Another is thermally induced from absorption in a thin sample in a Fabry-Perot interferometer [25]. Thin samples and filters can serve as both the medium and the resonator, and it is with this analogy we compare the absorption in the thin films of the SAL mirrors to the absorption in a thin sample. To this point, optical absorption due to absorption in mirror coating has not been reported. One reason for this is the unique condition that allows for this observation. The absorption must be highly localized so that the thin film can heat up and cool down rapidly and the cavity must have a narrow linewidth (high finesse) in order to resolve the small frequency shift caused by thermal expansion (on the order of Angstroms) [6]. The SAL resonator meets these requirements and hence allows for the first observation of optical absorption induced by mirror absorption.

6.3.5 Other Observations

Since the expansion was predominantly in the mirror substrate, the fused silica substrate can be said to have some thermal harmonic behavior. In suggesting this idea, I submit three graphs. As seen in Figure 6-6, there was variation in the frequency shift of the expanding cavity. Likewise there appeared to be some harmonic behavior in the frequency shift as a function of scan frequency, see Figure 6-7. More interesting, there were observed frequency shifts in the first sideband encountered during the cavity expansion. Thermal expansion is not likely to explain this phenomenon since the cavity field is much smaller than on resonance. However, it is my speculation that this can be explained by some residual substrate oscillations from the previous cycle. A similar oscillatory dynamic was observed in the expanding cavity lineshape. Portrayed in Figure 6-8 are the broadening of the sidebands and the modulations observed in the lineshape of expanding cavities.

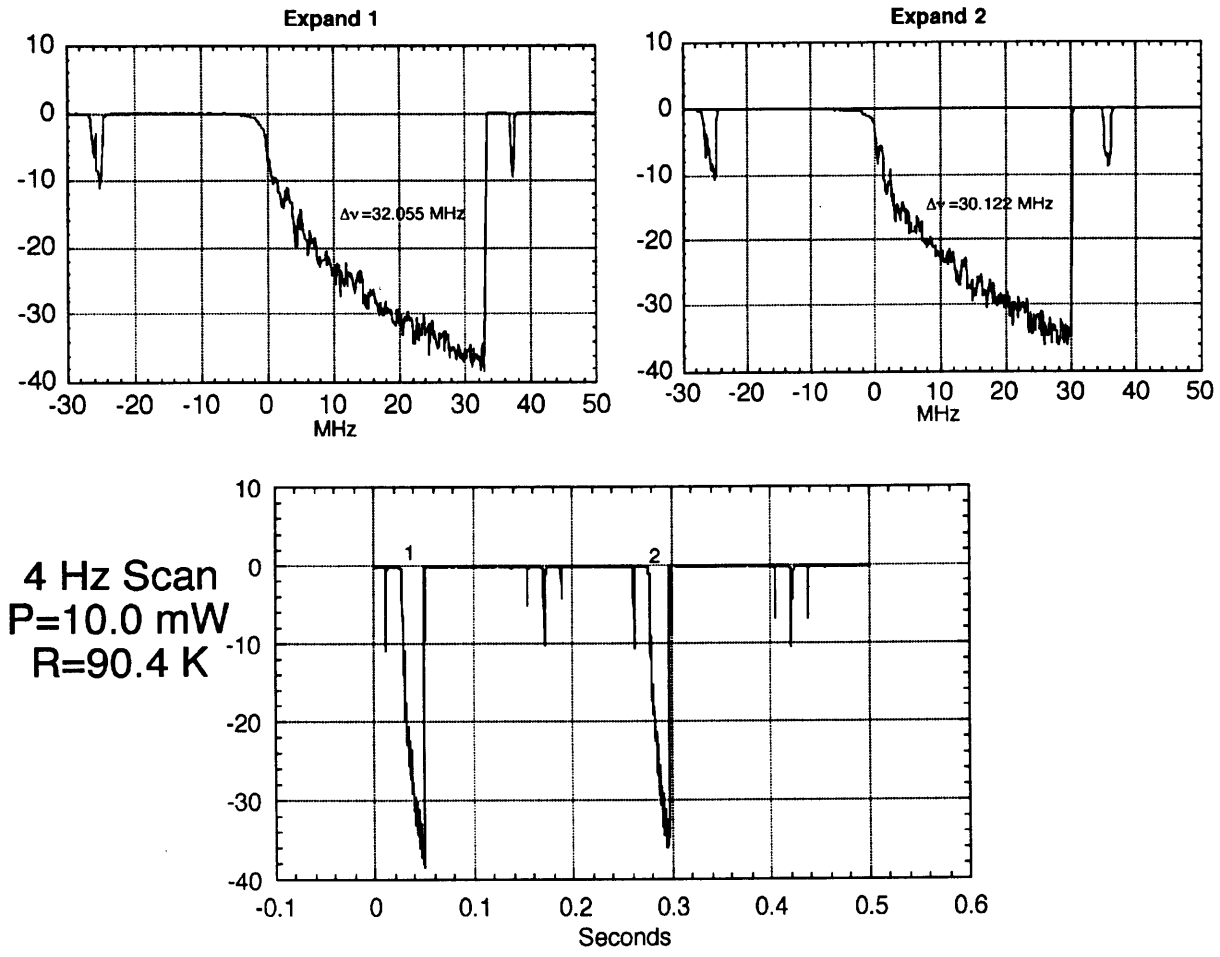

Figure 6-6: Two consecutive expanding cavity lineshapes. 4 Hz scan, P_{in}=10.0 mW.

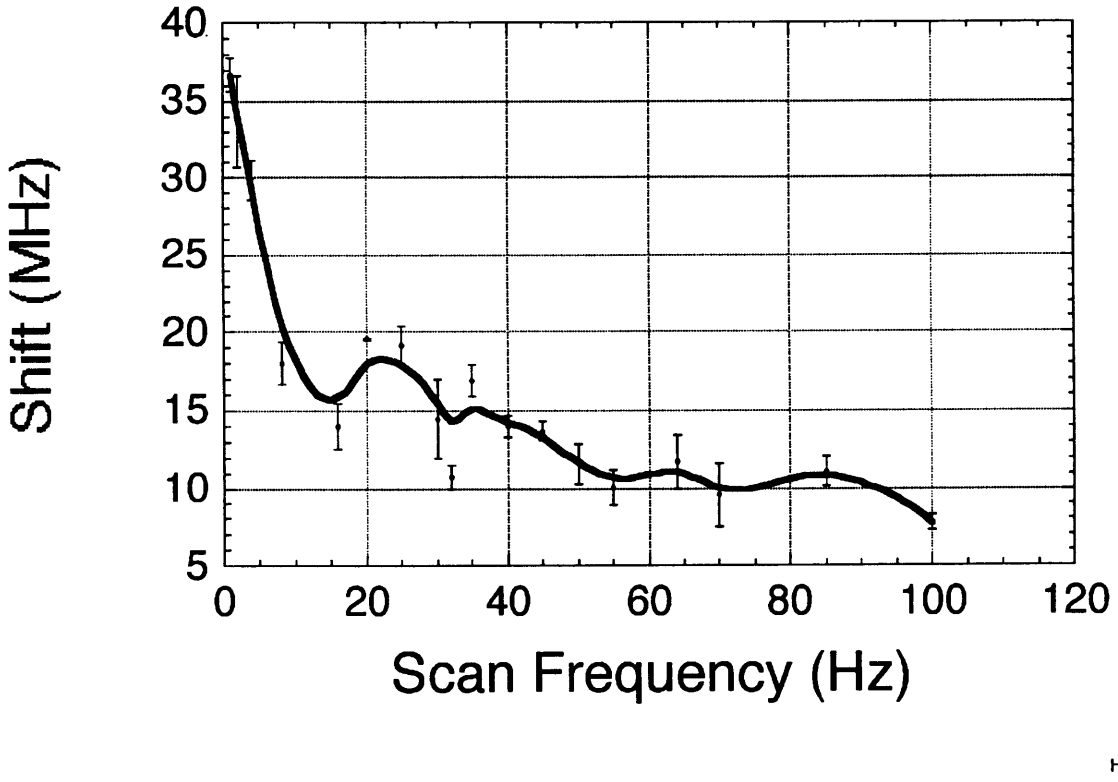

Figure 6-7: Smoothed fit to scan frequency versus averaged frequency shift. P_{in}=10.0 mW.

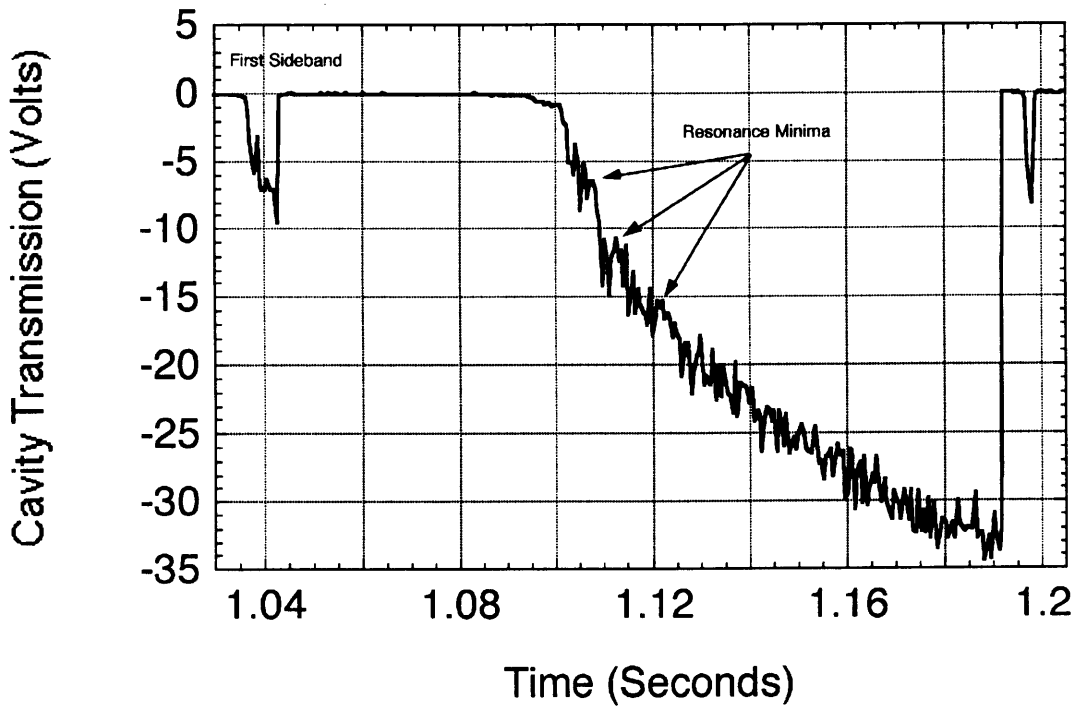

Figure 6-8: Expanding cavity lineshape. Demonstration of sideband broadening and modulation in lineshape. 4 Hz scan, P_{in}=10.0 mW.

Chapter 7

Scattering

Optical scattering is a broadly defined subject which needs specification to be discussed cogently. For example, scattering can refer to light's interaction with a surface, bulk material, contaminate imperfections, atoms, molecules or resonance effects such as Raman scattering [26]. In the treatment of optical losses in super-cavity mirrors, some assumptions may be made. First, because the amplitude of the electric field decays exponentially while traversing a dielectric stack designed for high reflectance, scattering at depths below say the first 10 layers is negligible when there are a total of 45 layers present. Second, scattering from atoms or molecules in the thin film results in energy deposited in the film; this is previously included in our definition of absorption. Consequently, we can focus our discussion of scattering to surface scattering events. Surface scattering results from rms fluctuations in the surface roughness, surface contaminates, and imperfections in surface figure.

While surface contaminates present obvious contributions to scattering loss, we deal with remedies later with mirror cleaning techniques. Consequently, we can further limit our scattering discussion to smooth and clean surfaces. In doing so, we define smooth surfaces as having height fluctuations (rms roughness) much less than the wavelength of the incident light. This condition is easily met with the super cavity mirrors which have rms roughness $\approx 1\mathring{A}$.

7.1 Scattering Theory

In the following, I present the simple model for surface scattering that is the foundation for determining the relationship between scattering and surface roughness for smooth and clean reflective surfaces. This relationship is determined by what has taken the name of Bennett's Scattering Equation [27]

$$S = \left(\frac{4\pi\sigma}{\lambda}\right)^2. \tag{7.1}$$

Here σ is the rms surface roughness and S is defined as the ratio of the scattered light to the reflected light. For highly reflective surfaces, this is equivalent to the scattering coefficient and is considered equivalent throughout this thesis.

Bennett's Scattering Equation is most often used in determining the surface roughness from a scatter measurement. While this was useful in early radar technology and in many current industrial applications, I intend to discuss its limitations in the SAL problem. A direct technique for measuring the scattering losses from super cavity mirrors is offered as an alternative.

7.1.1 Surface Scattering Model

Fourier analysis allows for the description of any surface height fluctuations in terms of the superposition of sinusoidal waves. As a result, scattering can be modeled from the refractive nature of light incident on a sinusoidal grating. Let a be the amplitude of the sinusoidal grating and f_g the grating frequency. If θ_i defines the angle of incidence in the plane of incidence, then the position of refracted orders, θ_n of the incident light follow the grating equation

$$\sin\theta_n = \sin\theta_i + nf_g\lambda \tag{7.2}$$

for n=0,1,2....

In the surface roughness analogy, a is the rms roughness given by $a = \sqrt{2}\sigma$, and f_g is the inverse distance between adjacent height fluctuations. From the grating analogy,

one observes that the location of diffracted orders depend on the grating frequency and the wavelength of the incident light, but not on the amplitude of the grating modulation nor the intensity of the incident light. However, the amplitude does determine the intensity of the diffracted orders. Using a scalar diffraction derivation in the limit of near normal incidence and smooth surface criteria, $(\frac{4\pi a}{\lambda}) \ll 1$), we can define the relative power P_n of the refracted orders from the one dimensional grating as [26]

$$P_n \propto [J_n(\frac{4\pi a}{\lambda})]^2 \simeq (\frac{2\pi a}{\lambda})^2 \tag{7.3}$$

So as a consequence, for the simple model of a sinusoidal scatting, we can determine the location and intensity of light refracted off of the surface. For a more realistic two dimensional grating of amplitude a_{xy}, the above equation reproduces Bennett's Equation with the simple substitution $a_{xy} = 4\sigma$. The same model is a useful starting point for the analysis of more chaotic and more realistic scattering surfaces.

7.1.2 Total Integrated Scattering and BSDF

In the past few decades, total integrated scattering (TIS) and bidirectional scatter distribution function (BSDF) have evolved for the measurement of scattering [26]. Both are derived with the goal of extracting information about the surface rms roughness from measured or collected scattered light. TIS describes scatter in terms of the collection of all scattered light from a smooth surface [28]. On the other hand, BSDF attempts to fully describe statistical rms roughness characteristics from the solid angle at which the scattered light is collected [29].

While I do not employ scattering measurements with specific collection solid angles, I introduce the terminalogy of BSDF because most recent literature discuss scattering in terms of the BSDF or bidirectional reflectance distribution function (BRDF). Important to BSDF are the power spectral distribution (PSD), which is a characterization of the surface roughness, the incident angle, and the solid angle in which the scatter is collected. The significance to these scattering laws is the

relationship between PSD and the BSDF. Knowing one leads to knowledge of the other.

These BSDF principles are particularly valuable to those who routinely operate comercial scatterometers. However, with such small SAL mirrors and without the precision machinery of scatterometers, the TIS is more appropriate to the scattering measurement of super cavity mirrors with TIS $\approx \left(\frac{4\pi\sigma\cos\theta_i}{\lambda}\right)^2$

7.1.3 Use of Total Integrated Scattering

In the measurement of S, my goal is to allow a scattering event to occur and capture the scattered photons while releasing the reflected laser beam. This can be done with an integrating sphere. The integrating sphere is similar to a spherical resonator in the sense that its interior walls are highly reflective R=99.2%, but, in contrast to a resonator, they are also diffusive. If a mirror is placed flush with the interior walls of the integrating sphere and light stikes the mirror, the scattered photons can either leak from the sphere or decay from optical damping. If the sphere was perfectly sealed, optical damping would be observed after about 100 bounces in the sphere. The sphere is not likely to be perfectly sealed, so it is safe to assume that optical damping is negligible compared to escaping photons. Suppose that the exit ports are limited to an incident aperture and a detection device. Then in steady state, the number of photons entering either exit can be estimated with a surface area ratio of the exit compared to that of the entire sphere. Then if the efficiency of the detector is known, determination of the total number of scattered photons can be made. The number of photons incident on the mirror is determined by the incident power and Planck's law ($E = h\nu$). As a result, with precise knowledge of the efficiency of the sphere and the detector, absolute measurments of S are made. Still , if detection calibration is not possible, then the relative calibration to another known quantity works as well. The alternative is to measure S compared to T, which can be measured separately. Both techniques are used and the results are discussed below.

7.2 Measurement of Scattering

As a result of the preceeding three measurements, the scattering losses can be determined to be 2.7 ± 0.1 ppm. As an attempt to verify this result, an additional measurement of scattering is proposed. Unlike the resonator based methods for measuring R, T, and A for a mirror pair, the scattering measurements are direct measurements of scattering losses for an individual mirror. The course of this error prone measurement takes on two approaches. One way is to measure scattering relative to transmission. If the transmission coefficient is known, then the scattering losses can be determined from the ratio. The advantage to this technique is that no absolute calibration of the detection system is needed. The other way is to make an independent measurement of the scattering. Determination of the efficiency of the detection system then leads to an absolute measurement of scattering.

The mirror high reflectivity provides conditions for measuring both transmission and scattering using an integrating sphere. In preliminary investigations, we directed a 791 nm laser beam normal to the reflective side of a mirror and inspected the distribution of photons reflected, scattered, and transmitted using an IR viewer. From the incident side, we observed an intense reflected beam and a back-scatter distribution that was maximum normal to the mirror and dropped in intensity at larger angles. From the transmission side, we observed a directional transmitted beam that is seen only when the viewer is aligned with the mirror-laser line, but we saw no forward scattering. The absence of forward scattering is due to the reflective mirror coating, which exponentially reduces any forward scattering which is already at a parts per million level. Consequently, total scattering measurements can be made by capturing photons on the incident side while allowing the reflected beam to escape. Similarly, transmission can be measured by capturing the photons on the transmitted side. An integrating sphere is ideally suited for such measurements.

7.2.1 The Modified Integrating Sphere

We modified a Shimadzu integrating sphere model UV-260 for the measurement of the scattering and transmission coefficients. In the modification, the integrating sphere is removed from its casing and the factory installed mirrors and PMT are removed. The integrating sphere is left in its purest form with three circular ports (ϕ=17 mm) and two rectangular ports (5 mm x 10 mm). All ports are in the same plane except the one circular port which sits at the botton of the sphere. Each port can be sealed. For most of these tests, only three ports are open at any given time: the mirror, input, and detection ports. The sphere has a radius of 3 cm, and its interior walls of barium sulfate are 99.2% reflective at 700 nm. By design, light entering the sphere assembles into an isotropic distibution of photons. This allows the correlation between the number of photon counting events with the number of photons scattered from or transmitted through a given mirror surface.

Two experimental precautions are warranted. First, in the scattering configuration (see Figure 7-1), sealing in the scattered photons is delicate given the need to release the reflected beam. A 2 mm reflective aperature is used at the sphere input. This is sufficiently large to pass the reflected beam which is focused at the aperature due to the mirror radius of curvature, and sufficiently small so that the number of escaping scattered photons is negligible ($\approx$.01%). Second, in the transmission configuration, non-normal incidence created from a large spot size can generate unusually large measurements for transmission. In order to match the cavity conditions, I focus the beam to the mode waist of the SAL cavity, about 40 μm. Beyond these two precautions, the physics of this experiment is simple.

To meet these challenges, I tried two different experimental configurations, refer to Figure 7-1. In each configuration, the incident laser beam is 791 nm and locked to the reference cavity of the Coherent 899 Ti:saphire laser. The distinction in the configurations is in the mirror location relative to the integrating sphere. For each configuration, a photon counting detection system is used. A Hamamatsu PMT Model R1635-02 is connected to a Stanford Research Systems(SRS) preamplifier, Model SR440 which feeds the signal to an SRS photon counter, model SR400. With

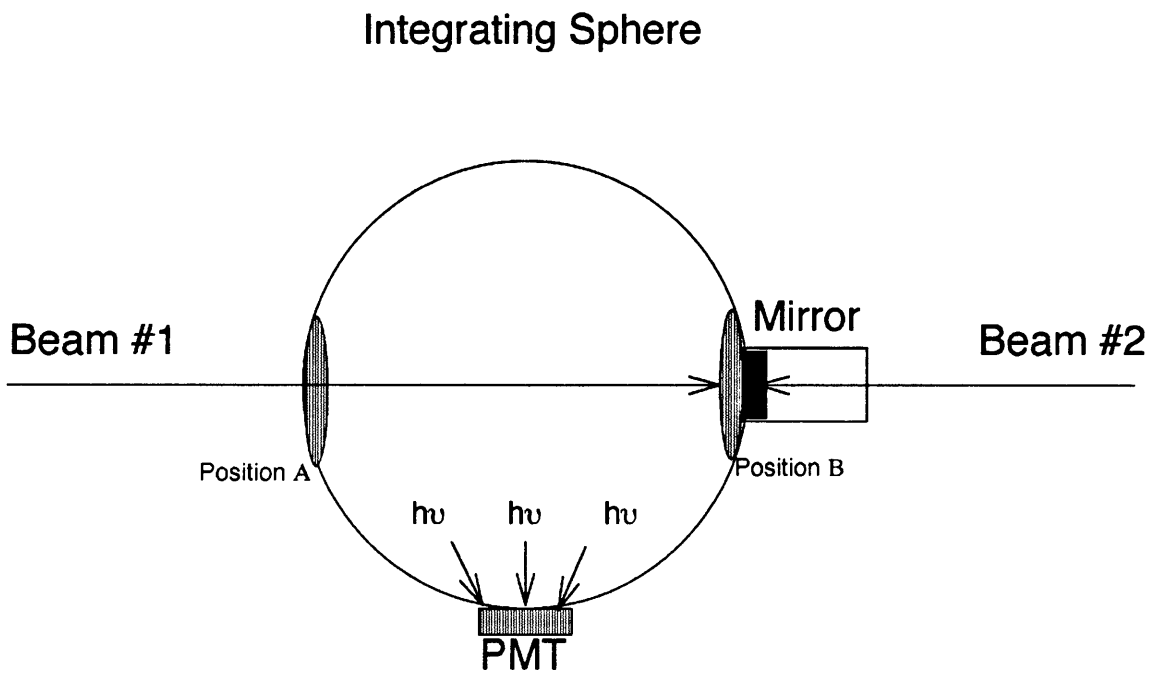

Figure 7-1: General scattering configuration for integrating sphere.

the PMT operating voltage set at 1500 Volts, the preamp was set to a gain of 25, and the photon counter was set at a discrimination level of -40 mV. Most often data was collected by counting for 5 second periods. The PMT detector face is positioned approximately 2 cm below the flush position of the interior barium sulfate wall at a 17 mm radius circular opening in the integrating sphere.

7.2.2 Scattering Configuration 1

In the Scatter 1 configuration, relative measurements are achieved with the mirror fixed at position B with two aligned counter-propagating colimated beams positioned at one location on the mirror. This is done using a lens (f=0.75 m) and a beam splitter so that the focus of each beam is approximately at the mirror thin film. Furthermore, the two beams are delicately aligned. Beam 1 is first positioned in the center of the mirror and normal to the mirror so that the reflected beam retraces the path of the incident beam. Beam 1 is also centered in the circular opening

(r=17 mm) of the sphere at Position A . Now beam 2 is introduced and aligned with beam 1. The utility of this configuration is that with minor adjustments both backscattering and transmission can be measured for the same spot location on the mirror. Backscattering is measured by blocking beam 2, closing the entrance hole at position A to 2 mm diameter, and heavily shielding the sphere in a black box with additional black material. At position A, I use a 0.5 inch thick piece of white teflon that is polished for high reflectivity on the inner side of the sphere while the outer side is painted black to prevent unwanted light from entering the sphere. The teflon aperature is further mounted on an x-y translation in order to position the aperature precisely at beam 1. The curvature of the mirror serves to focus (f=5 cm) the reflected beam 1 at nearly the location of the aperature (6 cm) so that the reflected beam is nearly guaranteed to escape from the integrating sphere. With the IR viewer, an additional check is made to see that the reflected beam is not striking the aperature. Without the necessary check with the IR viewer, inadvertant clipping of the reflected beam can result in unreasonably high backscattering measurments.

In measuring the transmission, beam 1 is blocked instead of beam 2, and the sphere entrance at position A is blocked with reflector, either a table mirror or a white polished teflon block. In early trials with this configuration, there was interest in allowing the transmitted beam to escape, leaving only the forward scattering to be measured in the sphere. Although this measurement can be complicated by photons entering the sphere from the transmission escape aperature, the results proved to substantiate the assumption that there is no forward scattering at the far end of the mirror. Consequently, by collecting all photons at the far end of the mirror, I am collecting only the transmitted beam.

Results for three mirrors are summarized below. Aside from the relative scattering measurements, these three mirrors are further characterized by finesse measurments with a common mirror and rms roughness measurements performed by Research Electro Optics, Inc. after coating [13]. Two mirrors provide good performance while the other performs poorly. These mirrors are labeled as M10, M6, and M3. When matched with a common mirror in previous cavity finesse measurements, the charac-

terizations were:

Mirror	Finesse	rms Roughness
M10	1.05 million	
M6	.936 million	0.56Å
M3	.445 million	1.12Å

The first important result is the variation in measurements as the spot location on the mirror is changed. To examine this effect, the two counter propagating beams were first positioned on the center of the mirror. Data was collected for that position, then the spot location was shifted slightly up, down, right, then to the left. The subsequent variation in the measurements for both T and S were 20%. The ratio of S/T for the averages of these five spot location has a large experimental error. For M10 for example S/T=4.3 $\pm$1.8. Let's make some assumption to see if this is reasonable. Assuming that mirrors in the same coating run have similar absorption, we can describe M10 with A=0.3 ppm, T$\approx$0.5 ppm, and from finesse, S=2.19 ppm. The measured T/S ratio would predict S=2.15$\pm$0.9 ppm which agrees nicely with the above ratio. There are problems with this rationale in that by using the finesse measurement with M10, I assume that the other mirror used in the cavity is identical to M10, and I also use S/T data that is averaged over many spot locations which is not the case with the resonator mirror. However, this still offers a satisfactory statistical confirmation of the absorption measurements.

As another verification, I use this value for S for M10 and make relative determination of the measured scattering for M3 and M6. By assuming A=0.3 ppm and using these values for S, I plot the theoretical finesse as a function of T for a cavity of identical mirrors. In Figure 7-2, I show this plot with actual finesse measurements with a common mirror. The measured finesse and expected values all fall with in the range of .421 ppm$<$ T $<$.524 ppm which again is in good agreement for the measured T from the SAL cavity. This is argument is intended as a verification of relative scattering measurments using all information available about these particular mirrors.

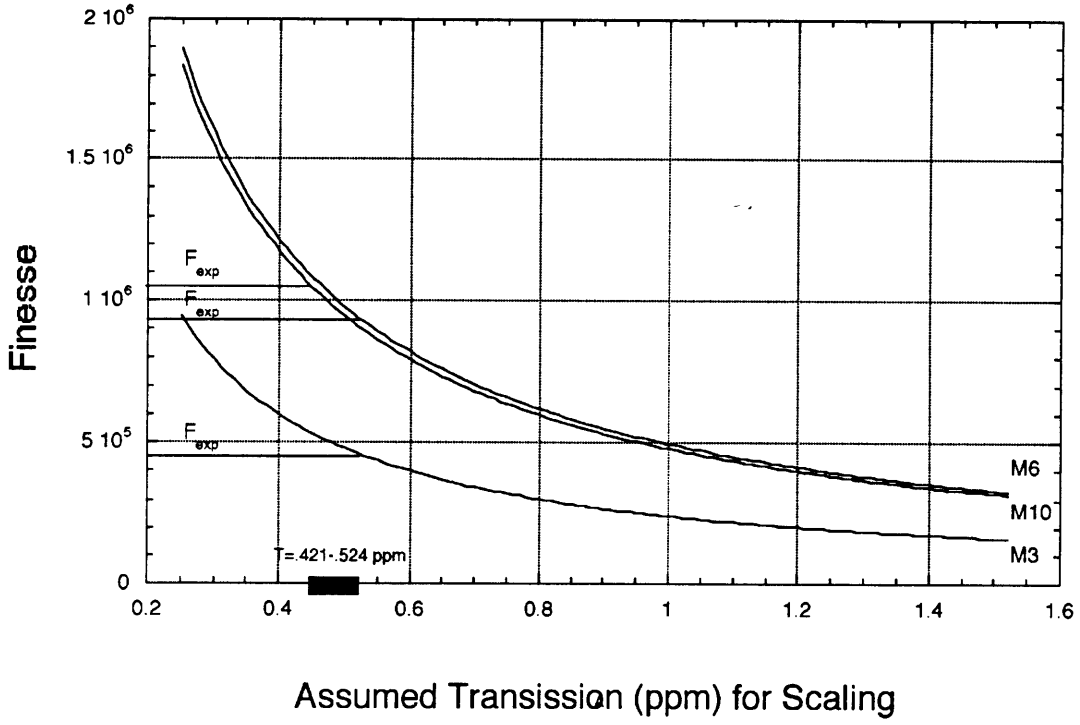

Figure 7-2: Theoretical finesse for assumed A=0.3 ppm and relative measurements of S. T is varied from 0.25 ppm to 1.5 ppm and measured finesse (F_{exp}) are depicted.

Another important result is the apparent disagreement between the measured S and the prediction using the surface roughness and Bennett's equation. One would expect that the scattering from M3 would be four times greater than the scattering from M6 because of the factor of two in the surface roughness. The PMT's quantum efficiency remains constant for scattering measurements of different mirrors. Scattering for two mirror can be compared with measurements of incident power and counts per second (cps). Then if we compare the position-averaged scattering data for M6 and M3, we find that scattering from M3 is only 2.0 $\pm$0.8 times greater than M6. Even with the large variation, this does not satisfy the predictions of the Bennett's equation. In fact, for the measured rms roughness, we would expect scattering loss to be 0.8 ppm and 3.2 ppm, respectively for mirrors M6 and M10. The issue at hand is whether the surface roughness measurements are accurate and/or the equation is suitable to for these conditions.

7.2.3 Scattering Configuration 2

The introduction of this new configuration was in response to an unexplainable observation that occured in configuration 1. As an attempt to make absolute measurements of S as well as T using the integrating sphere, I set out to measure the efficiency of the sphere detection system. I allowed a known laser power to enter the sphere and wished to calibrate the detection system. In principle, my hope was to simulate the mirror's transmitted light with a comparable power of direct attenuated laser light. The two light sources seemed equivalent. One is low powered light transmitted through a super-cavity mirror, and the other is low powered light transmitted through a series of neutral density filters.

Consistently, the determined detection efficiency using the direct laser led to absolute determination of T to be about 100 times larger than expected. The consequences of such a calibration led to even more unreasonable values for S, on the order of 300 ppm. So in a series of trail and error, configuration 2 was used such that instead of alternating between two counter propagating beams, there is just one incident beam traveling in the path of beam 1 with the mirror facing the beam but located at ei-

ther position A for the transmission measurement or position B for the scattering measurement.

To examine this observed contradiction, I changed a number of variables one at a time. These changes include varying the spot size of the beam on the mirror, the spot size of the direct laser, the polarization of the direct laser beam, and aperatures for both types of light. The light entering the sphere strikes a diffusive block as it is integrated into the sphere. These blocks were changed with different materials. I even displaced the the mirror by a few centimeters to nearly a meter outside of the integrating sphere to examine the mirror's geometric impact on the sphere when the transmission was measured. Additionally, the PMT was tested for linearity, and I disengaged the photon counter and sent the PMT signal directly to an anologue oscilloscope. Again, there was nothing to explain the discrepancy. In the end, while there were some corrections with these changes, none could explain the factor of 100 discrepancy.

Finally, the idea of separating the PMT from the integrating sphere came to mind. This would isolate the problem to either the PMT or to the sphere. The next step was to allow the two types of light to strike directly onto the PMT detector face. In doing so, I found that the differences remained, leading to the conclusion that the PMT views the two sources of light differently. This particular PMT was designed to operate in the visible regime, but there was no expectation that these two light sources would have inherent differences. However, recall that while the dielectric stack serves as a high reflector for 791 nm, it also serves as a filter at that wavelength. The conclusion is that the transmitted light carries a frequency component other than 791 nm for which the PMT is more sensitive. The caveat to this argument is that this other colored transmitted light must be very close to 791 nm because the variations remained even when the incident light was filtered with either a red color filter or an interference filter for 791 nm$\pm$1 nm.

Besides exposing the source of the discrepancy, another benefit to detaching the PMT from the integrating sphere was the determination of the integrating sphere efficiency. Using either of the types of light, the sphere efficiency was deterimed by

comparing the counts for light incident directly onto the detector to the situation with light went into the sphere with PMT attached. The following was discovered. Note that the data are presented in terms of counting efficiency, where the values were normalized to the incident power

Condition	Efficiency	Ratio
Transmission into PMT	$9.53x^{-5}$	
Laser into PMT	$6.38x^{-7}$	149
Transmission into sphere	$9.05x^{-7}$	
Laser into sphere	$9.22x^{-9}$	98

Then the sphere efficiency is 0.95% for transmitted light and 1.44% for direct laser. Efficiency is determined by ratio of counted photons to available photons scattered in the integrating sphere.

While the present PMT's distinguishing ability has been instructive about the peculiar nature of the transmitted light, the further pursuit of such scattering measurements rests with a new PMT that will see all photons equally. A PMT designed for operation in the IR is bested suited for this measurment. The new PMT is a Hamamatsu model R943-02 which is actively cooled by a refrigeration system to -20 °C. At an operating voltage of 1500 volts, the discrimination level was determined to be -27mV. This was determined by scanning the discrimination level in order to first select a region for single photon counting events. Once this region was determined, the specific discrimination voltage was determined by selecting the most sensitive level while maintaining linearity in the PMT. This was done by attenuating the incident power by a factor of 10 and ploting the ratio of counts for the two intensities versus the discrimination level, see Figure 7-3.

With the new PMT, the transmitted and direct laser beams were compared first with incidence directly onto the PMT. For equal incident powers, there was equal detection. Next, the PMT was configured with the integrating sphere. In this configuration, the measurement was extremely sensitive to proper shielding and to the elimination of any clipping of the reflected beam. Typical measurements of scattering

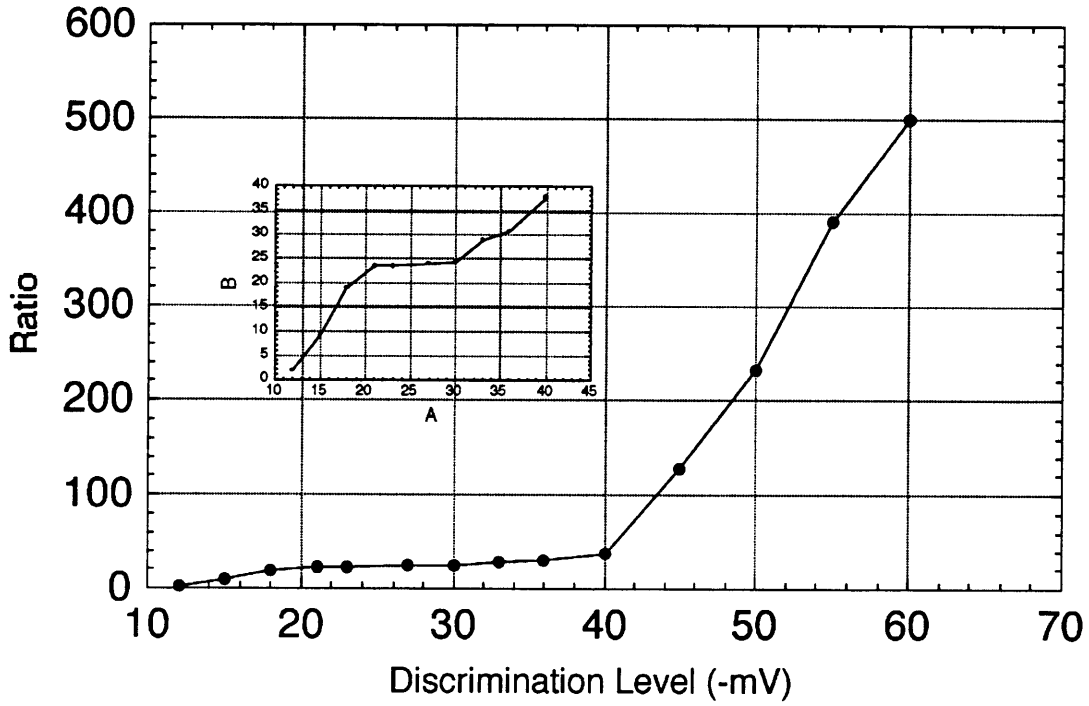

Figure 7-3: Determination of PMT discrimination level. V=-27mV.

result in values 5-6 times greater than expected from earlier finesse measurements. For example, mirror M10 should have scattering on the order of 2.5 ppm yet the measurement in this case was 13 ± 1 ppm.

The scattering measurements with the integrating sphere proved to be unreliable in the absolute measurement and questionable in the measurement relative to T due to the differences observed in transmitted light and incident light. However, these tests still show promise with better experimental procedures. More importantly, the use of the integrating sphere exposed an inherent difference between the light incident onto a super cavity mirror and the light transmitted through the mirror. It also offered a simple platform for measuring the mirror transmission using the direct incidence techniqued discussed in Section 3.2. Finally, it demonstrated disagreement between the measured S and the prediction using the surface roughness and Bennett's equation

.

Chapter 8

Discussion and Mirror Optimization

Recall that the goal of this work is to increase g, the coupling constant. The primary route to higher coupling is through higher finesse. In this chapter, I examine the measured SAL mirror characterizations and conclude that scattering is the dominant loss mechanism in super cavity mirrors. In targeting scattering, I examine the available information to develop a strategy for minimizing scattering. Some of the strategies are then experimentally tested. Finally, I offer a practical discussion of changes in T and resonator design that can increase g.

8.1 Analysis

The characterization of the super cavity mirrors allows us to identify the parameters that most hinder their performance in the SAL experiment. The intent is to maximize R by minimizing T, A, and S. From the measurements of R, T, A, and S, we can fully describe the mirrors in the existing SAL super cavity. These values are presented below in Table 8.1. Nearly ten times larger than absorption, scattering is the dominate lo mechanism. Clearly, the largest potential gain in R is achievable through the reduction of S. The question is how to make these reductions given the current manufacturing technology.

Finesse	$9.0 \pm 0.1 \times 10^5$
R	$0.99999651 \pm 0.00000004$
T	0.5 ± 0.1 ppm
A	0.3 ± 0.1 ppm
S	2.7 ± 0.1 ppm

Table 8.1: Summary of SAL mirrors R, T, A, and S.

8.1.1 Initial Assumptions

In order to interpret these results and to develop our next step, we make some preliminary assumptions.

1. Scattering results from both surface rms roughness fluctuations and interlayer defects in the dielectric stack.

2. Mirror surface roughness is correlated to pre-coating surface roughness of the substrate.

3. Optimum conditions for super polishing are on a flat surface; conditions degrade as the curvature is reduced beyond a threshold radius of curvature.

4. Since the magnitude of the steady state electric field in a dielectric stack is maximized at the low to high index boundaries, absorption and inter-layer scattering are most affected at these locations.

5. The effect of these absorption and scattering locations is limited to the first few film layers because the magnitude of the electric field decays exponentially through the length of the dielectric stack.

6. Increases in the number of layers is likely to increase scattering because there would be statistically more interlayer scattering opportunities [13].

7. Increases in the number of layers will not substantially change this exponential decay length in mirrors with already 45 layers.

8. Optical absorption in thin films is a characteristic of the extinction coefficients of their bulk material.

9. There are no other dielectric materials with lower extinction coefficient that Ta_2O_5 and SiO_2.

10. Increases in the number of layers are not likely to change the mirrors' absorption

	Best SAL	Current SAL	Caltech[4]	LIGO[30][13]	ZEISS[13]
Cavity Use	Micro Laser	Micro Laser	Micro Laser	Interferometer	Gyro
Finesse	1.3 million	.9 million	1.9 million	.3 million	(4.5 million)
1-R	2.4 ppm	3.49 ppm	1.65 ppm		0.7 ppm
T		0.5 ppm	0.5 ppm		
A		0.3 ppm			
S		2.7 ppm			
A+S		3.0 ppm	1.2 ppm	1.0 ppm	(0.4)
T+A+S	2.4 ppm	3.49 ppm			0.7 ppm
Wavelength	791 nm	791 nm	850 nm	514 nm	633 nm
Number of Layers	45	45	45		
Mirror radius	10 cm	10 cm	17/100 cm		$\gg$ 100 cm
Substrate	FS	FS	FS/BK7	FS	FS

Table 8.2: Summary of recent reports of low loss. FS is fused silica.

characteristics.

11. Theory for transmission reduction is accurate. Each additional H-L pair reduces T by $(n_L/n_H)^2$.

8.1.2 Reports of Low Loss

In developing the strategy for minimizing scattering loss, we also look to other notable reports of low loss conditions to identify the contributing factors. Table 8.2 is a partial list of recent low loss observations from mirrors manufactured by Research Electro Optics, Inc. with Ta_2O_5 and SiO_2 thin films. Our investigation of scattering minimization rests with analysis of our data, the above assumptions, and the other reports of low loss. Some general observations are made from this information. The notable differences in the reports of lower loss are in the mirror functional use, wavelength, and substrate. Comparing the use of the gyro and the interferometer, the Ligo project designs for higher T than Zeiss, which was designed for 0.3 ppm transmission. Consequently, there are about 10 more layers in the Zeiss mirrors. Let's compare their $A + S$ and assume A equal for both. Then there is no appreciable difference in scattering for the Zeiss mirrors with larger number of layers. Contradicting assumption number 6, this gives credence to increasing the number of layers at no expense

in scattering.

Next, compare wavelength dependence. As reported elsewhere [4], scattering in thin films does not strictly obey the Rayleigh $1/\lambda^4$ dependence. Likewise, predictions from Bennett's Equation are not supported by the reports of low loss. Demonstrated in the table, lower scattering is observed in the visible regime than in the IR. This is yet unexplained and warrants further examination.

Finally, consider the SAL and the Caltech mirrors. Both are used for the same purpose at nearly the same wavelength. The design parameters were identical: same thin film materials, same number of layers, and same design for transmission (0.5 ppm). The distinct difference is in the substrate. As noted in Chapter 4, the Caltech substrates used for measuring finesse of 1.9 million were manufactured and super polished by General Optics. To explore this possible explanation for higher finesse, we sent our REO substrates to General Optics for comparison. No distinction in superpolishing could be made [31]. However, in Chapter 7 scattering data suggested some disagreement between the measured rms surface roughness and the predicted scattering from Bennett's Equation. The roughness characterization at sub-Angstrom level is pushed to the limits of this interferometry technology and is admittedly subject to error [13]. In fact, such characterizations can be wavelength limited such that a measurement of surface roughness at one wavelength cannot be used in Bennett's Equation to determine the scattering at another wavelength [26].

Considering the status of the current SAL mirrors, we can first conclude that absorption in our mirrors is reasonably minimized given the optical properties of the thin films and the fact that absorption occurs in only the first few layers of the mirrors. Second, while the elimination of interlayer defects rests in technological advances, surface scattering minimization can be achieved through improvements in the mirror surface roughness of the mirror or through enhanced cleanliness. Third, there exists an optimized T that can be reduced to a threshold for acceptable signal to noise ratio. Consequently, our attention is turned to the minimization of S and the optimization of T.

8.2 Minimization of Scattering

The minimization of scattering is investigated in regards to surface contaminants and surface roughness. If scattering is a result of dirty mirrors, then a simple solution would be to clean the mirror surface. This is discussed below using a centrifuge, while roughness contributions to scattering are later investigated as a function of mirror radius of curvature.

8.2.1 Minimization of Surface Contaminants

In order to investigate the effects of surface contaminants, an alternative cleaning techniques was employed. As discussed in Reference [32], mirrors can be cleaned with the assistance of centrifugal force. For this investigation, a modified medical centrifuge was used for mirror cleaning. The technique is to mount an individual mirror on a centrifuge in such a way that the mirror spins around its axis at 3,000 rpm. The mirror is then flushed with a cleaning solution while a moist cotton Q-tip is applied to the rotating mirror. The spinning motion serves to lift contaminants from the mirror (while the Q-tip is applied) and to throw the debris and solvent away from the substrate surface (when the Q-tip is removed).

In this investigation, an IEC Medispin medical centrifuge was modified by removing its cover assembly and test tube rack. A three pronged mirror mount was connected to the exposed centrifuge shaft. For cleaning solutions, I used many sequences of methanol, acetone, isopropyl alcohol, and distilled water. Additionally, Q-tips and finely folded lens tissue were used as applicators. Cleaning was done in an enclosed ventilation system with carefully cleaned handling devices, and latex gloves were always used when working with the mirrors. Initial cleanliness was inspected using an Olympus X250 darkfield microscope with mirror samples illumination from the bottom. The comparison of cleaning techniques was made with finesse measurements of mirrors cleaned with the same technique. In all variations of different ordering of solvents with either applicator or with no applicator, I found no enhancement in cavity finesse compared to mirrors repeatedly cleaned using a common lens tissue swipe.

However, in comparing the two techniques, the centrifuge provides a uniformly clean central region of the mirror surface, while the tissue swipe is subject to human error that can leave the center uncleaned and the sides of the swipped path left with a trail of residue.

Based on microscope observations of the mirrors cleaned with the centrifuge, some additional remarks can be made. First, the flushing of mirrors with distilled water as the last cleaning step resulted in virtually no observed residue on the mirrors, while the other more quickly evaporating solvents always left some circular residue pattern near the outer edge of the mirror. Second, it was best to apply the last cleaning solution to the mirror while it was still stationary. This eliminated the splash associated with the application to a spinning mirror. Finally, improper handling of applicators during the spinning of the mirror can result in mirror damage. This was observed with lower measured finesse. Two of the 30 mirrors tested were damaged in some way. Since the mirrors are held to fairly sanitary laboratory conditions, dust particles are the most likely surface contaminant. Consequently, it is best to just flush the mirrors with the cleaning solution and to use no applicator such as the Q-tip.

8.2.2 Minimization of Surface Roughness

Given the parameters of the tables above and our concerns about the correlation between scattering and measured surface roughness, we set out to test a selected number of mirror parameters. Three primary investigations were done using finesse as a means of comparison. Mirrors are clamped in place rather than glued as with the SAL resonator. First, we wanted to compare the performance of BK7 and FS substrates. Second, we wanted to compare the impact of mirror substrate radius of curvature on mirror surface roughness. Third, a comparison of mirrors with wedge and bevel and those without was compared. To do this, the mirrors listed in Table 8.3 were purchased from REO for our testing. Additionally, ten wedged 10 cm fused silica substrates were coated simultaneously as a reference to the existing SAL mirrors.

While just limited testing has been perform on four to six mirrors of each substrate at 100 cm and 10 cm, the preliminary results are that there is no reduction of loss

Substrate	Radius of Curvature
FS	5cm
BK7	10cm
FS	20cm
BK7	20cm
FS	50cm
BK7	50cm
FS	100cm
BK7	100cm

Table 8.3: New mirrors used for testing finesse dependence on substrate and radius of curvature.

from mirrors with the larger radius of curvature. In fact, a pair of 5 cm fused silica mirrors were tested with equivalently high finesse. In comparing the surface roughness measurements of substrates prior to mirror coating, we found no correlation between finesse and measured rms roughness between 0.40-0.67 Angstroms. Finally, in comparing the new mirrors that had no back surface wedge to the old substrate with the wedge, there was no observed difference. While these tests do not lend to the reduction of scattering, they eliminate some of our early assumptions as untrue, and provide insight into other possibilities of increasing g. Additional tests of both types of substrates were done to see if spot location variations would greatly change the finesse. Typically, four spot were chosen on the mirror by tilting one of the cavity mirrors slightly and realigning the probe beam to the TEM_{00} mode. There was only a 10 % variation in the finesse.

8.3 Optimization of T and Cavity Parameters

Additional gains in g can be made with the optimization of T and other cavity parameters. In the sections below, I assumed finesse of 2 million to discuss changes in T and cavity design. I present a discussion of how far we can reasonably reduce T and examine the impact of increases in the mirror radius of curvature.

8.3.1 Optimization of T

From the Zeiss gyro mirrors, we see that there may be gains to be made with reduced transmission at no cost to scattering and absorption. The optimization of T, requires the lowering of T to a reasonably detectable signal. The detection scheme for the SAL output is an avalanche photodiode in the photon counting mode of operation. While the APD dark counts are only 300 cps, noise can still be appreciable given the laboratory conditions with multiple lasers, electronics, and a barium oven nearby. As seen from the SAL output, maximum background noise is around 16,000 cps (200 counts per 12.5 ms).

The SAL cavity throughput is T/(T+A+S) so that the laser output S' is expressed by [1]

$$S' = \frac{1}{2}\langle n\rangle \Gamma_c \left(\frac{T}{T+A+S}\right)\eta \tag{8.1}$$

where $\langle n\rangle$, Γ_c, and η are the mean photon number, the cavity linewidth, and the efficiency of the detection system. With the hypothetical condition of finesse of 2 million and improved detection efficiency with higher $\langle n\rangle$, we can further suggest an acceptable throughput of 10%. Then 1-R would equal 1.6 ppm and the lowest acceptable T would be 0.16 ppm. This allows for just minor change in mirror design with the addition of 1 more thin film pair (47 total layers).

8.3.2 Cavity Parameters

As a last parameter for change that will generate an increase in the coupling constant, we turn to the mode volume. Already, we have seen in Chapter 2 that there is an optimum cavity length for a given cavity finesse. Again, for a cavity of finesse 2 million, the change in optimum cavity length would to 0.5 mm. This change can be added to the experimental observation that the radius of curvature can be reduced from 10 cm to 5 cm without reduction of finesse. If these geometric changes were incorporated into the SAL resonator we would see a factor of 2 increase in the coupling constant, thus raising g to 1.0 radians. Although this is far below the necessary condition sought at the outset of this work, we now have new information with which

to design the next generation of the super cavity mirrors.

Chapter 9

Conclusion

This thesis introduced new methods for measuring transmission and absorption coefficients and reported the first observation of optical bistability from absorption in mirror thin films and the first partitioning of loss into scattering and absorption.

The motivation for this thesis was to augment our understanding of loss mechanisms in super cavity mirrors in order to develop strategies for increasing cavity finesse and the coupling constant. The first step was to fully characterized the mirrors in terms of R, T, A, and S. Measuring R with a ringdown technique, this work set out to develop a new means for measuring T with the modified ringdown throughput. The result was a simultaneous measurements for R and T with reflection and transmission, respectively determined from the temporal behavior and from the amplitude of the ringdown cavity output. Still using the same experimental configuration, A was measured by examining the thermally induced expansion of the mirrors during slow cavity scan scans. As a result, the measurements of R, T, and A then determine S and allow for the full characterization of the super cavity mirrors. Nearly ten times larger that absorption, scattering was identified as the primary mirror loss mechanism.

With this information, we focused our attention to scattering minimization. Mirror cleaning and surface roughness were investigated with no improvements in cavity finesse. The highest finesse measured to date is 1.34×10^6 with a 10 ppm fused silica mirror designed for 0.5 ppm transmission. However, valuable information was gathered along the way.

9.1 Summary of Results

Below is a list of significant findings.

1. Scattering is the dominant loss mechanism in super cavity mirrors.

2. Scattering and substrate surface roughness measurements less than 1 $\mathring{A}$ are not well correlated with Bennett's Equation at 791 nm.

3. Scattering does not strictly obey the Rayleigh $1/\lambda^4$ relation.

4. The lowest reported loss is in the visible spectrum.

5. Movement of spot location on mirrors results in a maximum of 10% variation in finesse, thus spoiling the notion of a mirror sweet spot.

6. There are no increases in mirror losses created from changes in radius of curvature from 100 cm to 5 cm.

7. There may be no added scattering losses with added layers of thin film pairs.

8. The super cavity mirror transmission is not spectrally identical to the incident light.

9. There is no evidence that lower loss can be achieved with BK7 substrates.

9.2 Future Studies

While increased finesse was not achieved, the realization of mirrors with lower loss may be just beyond our grasps. Certainly, the minute loss reported in the Zeiss gyro mirror suggest the possibility of a cavity finesse of 4.5 million. This would satisfy our needs.

For the time being, the next step in the SAL experiment would be to employ the 5 cm radius of curvature mirrors. For the future, investigations are warranted in the reduction of the design specification of T, possible selection of another atom whose transition is in the visible regime, and further reduction of mirror radius of curvature.

Unquestionably, significant reduction of loss will only be found in the reduction of scattering. The most unusual observations occur from scattering wavelength dependence. Consequently, this should be the priority for further investigations to

understand and minimize scattering loss.

Bibliography

[1] K. An, Ph.D. thesis, Massachussetts Institute of Technology, 1995.

[2] R. Berman, *Cavity Quantum Electrodynamics*, 1st ed. (Harcourt Brace & Company, San Diego CA, 1994).

[3] K. An, C. Yang, R. Dasari, and M. Feld, Optics Letters **20**, 1068 (1995).

[4] G. Rempe, R. Thompson, J. Kimble, and R. Lalezari, Optics Letters **17**, 363 (1992).

[5] Z. Wu *et al.*, SPIE Proccedings **2714**, 465 (1996).

[6] K. An *et al.*, Submitted to Optics Letters .

[7] C. Yang and K. An, Submitted to Physical Review Letters .

[8] K. An, Physical Review Letters **73**, 3375 (1994).

[9] H. Macleod, *Thin-film optical filters*, 2nd ed. (Adam Hilger Ltd, Bristol, 1986).

[10] Q. Zhao and Z. Fan, SPIE Proceedings **2214**, 331 (1996).

[11] R. Stanley and K. Andrew, Journal of Optical Society of America **54**, 625 (1964).

[12] C. Carniglia and J. Apfel, Journal of Optical Society of America **70**, 523 (1980).

[13] R. Lalezari, Research Electro Optics, Inc., 1855 South 57th Court, Boulder, Colorado 80301: private communication.

[14] A. Yariv, *Optical Electronics*, 3rd ed. (CBS College Publishing, New York, NY, 1985).

[15] J. Poirson, F.Bretenaker, M. Vallet, and A. LeFloch, Annales de Physique **20**, 607 (1996).

[16] M. Commandre and P. Roche, Applied Optics **35**, 5021 (1996).

[17] K. An, R. Dasari, and M. Feld, Applied Physics Letters **66**, 2162 (1995).

[18] B. Dion, EG&G ORTEC, Mississauga, Ontario L5N 2M2 , Canada: private communication.

[19] J. Lambropoulos, Journal of Applied Physics **66**, 4230 (1989).

[20] M. Ohring, SPIE Proccedings **2114**, 624 (1994).

[21] M. Commandre, L. Bertrand, G. Albrand, and E. Pelletier, SPIE Proceedings **805**, 128 (1987).

[22] M. Reichling, E. Welsch, and E. Matthias, SPIE Proceedings **1781**, 205 (1993).

[23] P. Roche *et al.*, Applied Optics **35**, 5059 (1996).

[24] A. Gozzini, Journal of Optical Society of America **B2**, 1841 (1985).

[25] H. Gibbs, *Optical Bistability: Controlling Light with Light* (Academic Press, New York, NY, 1985).

[26] J. Stover, *Optical Scattering, Measurement and Analysis*, 2nd ed. (SPIE, The International Society for Optical Engineers, Bellingham, WA, 1995).

[27] J. Bennett, Thin Solid Films **123**, 27 (1985).

[28] J. Neu, SPIE Proceedings **1995**, 101 (1993).

[29] T. Schiff *et al.*, SPIE Proceedings **1995**, 121 (1993).

[30] D Coyne, IEEE Proceedings **3196**, 31 (1996).

[31] K. Scribner, General Optics, Inc., 544 Flinn Ave., Moorpark, California 93021: private communication.

[32] J. Brown, SPIE Proceedings **1995**, 80 (1995).